

1 **Impact of topography on black carbon transport to the southern Tibetan**  
2 **Plateau during pre-monsoon season and its climatic implication**

3 <sup>1</sup>Meixin Zhang, <sup>1</sup>Chun Zhao\*, <sup>2,3</sup>Zhiyuan Cong, <sup>1</sup>Qiuyan Du, <sup>1</sup>Mingyue Xu, <sup>1</sup>Yu Chen, <sup>4</sup>Ming  
4 Chen, <sup>1</sup>Rui Li, <sup>1</sup>Yunfei Fu, <sup>1</sup>Lei Zhong, <sup>3,5</sup>Shichang Kang, <sup>6</sup>Delong Zhao, <sup>6</sup>Yan Yang

5  
6  
7 <sup>1</sup>School of Earth and Space Sciences, University of Science and Technology of China, Hefei,  
8 China

9 <sup>2</sup>Key Laboratory of Tibetan Environment Changes and Land Surface Processes, Institute of  
10 Tibetan Plateau Research, Chinese Academy of Sciences (CAS), Beijing 100101, China

11 <sup>3</sup>CAS Center for Excellence in Tibetan Plateau Earth Sciences, Institute of Tibetan Plateau  
12 Research, CAS, Beijing 100101, China

13 <sup>4</sup>National Center for Atmospheric Research, Boulder, CO, USA

14 <sup>5</sup>State Key Laboratory of Cryosphere Science, Northwest Institute of Eco-Environment and  
15 Resources, CAS, Lanzhou 730000, China

16 <sup>6</sup>Beijing Weather Modification Office, Beijing 100101, China

17  
18 Manuscript for submission to Atmos. Chem. Phys.

19  
20  
21 \*Corresponding author: Chun Zhao (chunzhao@ustc.edu.cn)

22  
23  
24 **Key points:**

25 1. The black carbon (BC) transport across the Himalayas can overcome a majority of mountain  
26 ridges, but the valley transport is much more efficient during the pre-monsoon season.

27 2. The complex topography results in stronger overall crossing-Himalayas transport during the  
28 study period primarily due to the strengthened efficiency of near-surface meridional transport  
29 towards the TP, enhanced wind speed at some valleys, and deeper valley channels associated  
30 with larger transported BC mass volume.

31 3. The complex topography generates 50% higher transport flux of BC across the Himalayas  
32 and 30-50% stronger BC radiative heating in the atmosphere up to 10 km over the Tibetan  
33 Plateau (TP) than that with the smoother topography, which implies that global climate models  
34 with relatively coarse resolution may introduce significant negative biases in estimating BC  
35 radiative forcing over the TP due to smooth topography.

36 4. The different topography also leads to different distributions of snow cover and BC forcing  
37 in snow over the TP.

39 **Abstract**

40 Most of previous modeling studies about black carbon (BC) transport and impact over the  
41 Tibetan Plateau (TP) conducted simulations with horizontal resolutions coarser than 10 km that  
42 may not be able to resolve well the complex topography of the Himalayas. In this study, the  
43 two experiments covering entire Himalayas with the Weather Research and Forecasting Model  
44 coupled with chemistry (WRF-Chem) at the horizontal resolution of 4 km but with two  
45 different topography datasets (4-km complex topography and 20-km smooth topography) are  
46 conducted for pre-monsoon season (April, 2016) to investigate the impacts of topography on  
47 modeling the transport and distribution of BC over the TP. Both experiments show evident  
48 accumulation of aerosols near the southern Himalayas during the pre-monsoon season,  
49 consistent with the satellite retrievals. The observed episode of high near-surface BC  
50 concentration at the station near the Mt. Everest due to heavy biomass burning near the  
51 southern Himalayas is well captured by the simulations. The simulations indicate that the  
52 prevailing up-flow across the Himalayas driven by the large-scale westerly and small-scale  
53 southerly circulations during the daytime is the dominant transport mechanism of South Asian  
54 BC into the TP, and is much stronger than that during the nighttime. The simulation with 4-km  
55 topography resolves more valleys and mountain ridges, and shows that the BC transport across  
56 the Himalayas can overcome a majority of mountain ridges but the valley transport is more  
57 efficient. The complex topography results in stronger overall crossing-Himalayas transport  
58 during the simulation period primarily due to the strengthened efficiency of near-surface  
59 meridional transport towards the TP, enhanced wind speed at some valleys, and deeper valley  
60 channels associated with larger transported BC mass volume. This results in 50% higher  
61 transport flux of BC across the Himalayas and 30-50% stronger BC radiative heating in the  
62 atmosphere up to 10 km over the TP from the simulation with 4-km complex topography than  
63 that with 20-km smoother topography. The different topography also leads to different  
64 distributions of snow cover and BC forcing in snow. This study implies that global climate  
65 models generally with even coarser resolutions than 20 km and therefore relatively smoother  
66 topography may introduce significant negative biases in estimating light absorbing aerosol  
67 radiative forcing over the TP.

68

69

70

71

72

## 73 **1. Introduction**

74 The Tibetan Plateau (TP) is the highest plateau in the world with an average elevation  
75 over 4 km and an area of approximately  $2.5 \times 10^6 \text{ km}^2$ , known as the world's third pole (Qiu,  
76 2008), and its enormous dynamic and thermal effects have a huge impact on large-scale  
77 atmospheric circulation through the energy exchange with the atmosphere especially the  
78 troposphere, such as Asian monsoon (e.g., Ye and Wu, 1998; Duan and Wu, 2005; Wu et al.,  
79 2007, 2012a; Boos and Kuang, 2013; Chen and Bordoni, 2014; He et al., 2019; Zhao et al.,  
80 2019). In addition, the glacial melting water of TP is one of the important sources of water  
81 resources of the Indus River, Ganges River, Yangtze River, and Yellow River in Asia (e.g.,  
82 Singh and Bengtsson, 2004; Barnett et al., 2005; Immerzeel et al., 2010; Lutz et al., 2014).  
83 Previous studies found aerosols in the atmosphere over/around the TP could change the  
84 regional climate of Asia (e.g., Qian et al., 2011, 2015; Lau et al., 2017, 2018). Model  
85 simulations showed that the absorptive aerosols changed the surface radiative flux over the TP  
86 by  $5\text{-}25 \text{ W m}^{-2}$  during the pre-monsoon season in April and May and led to the changes in  
87 summer monsoon circulations (Qian et al., 2011). Meanwhile, aerosol may affect the  
88 atmosphere by modulating the vertical structure of cloud and precipitation around the TP, and  
89 thus change the distribution of atmospheric latent heat around the TP, which is the main driving  
90 force of regional atmosphere circulations (e.g., Li et al., 2010, 2017, 2019). Moreover, when  
91 absorbing aerosols settle on the snow-covered areas, they will blacken the surface of snow  
92 cover and glacier to a large extent (e.g., Hansen and Nazarenko, 2004; Ramanathan and  
93 Carmichael, 2008; Lau et al., 2010, 2018; Lee et al., 2013; Zhang et al., 2017, 2018), reduce  
94 the snow albedo so as to absorb more solar radiation and cause the consequences of accelerated  
95 melting (e.g., Ramanathan et al., 2007; Ming et al., 2009; Yasunari et al., 2010; Ji et al., 2015;  
96 Zhang et al., 2015). According to the Intergovernmental Panel on Climate Change Fifth  
97 Assessment Report (IPCC AR5), the radiative forcing caused by the important component of  
98 absorbing aerosols, black carbon (BC), on the surface snow is  $0.04 \text{ W m}^{-2}$  ( $0.02\text{-}0.09 \text{ W m}^{-2}$ )  
99 on global average, and the regional forcing (such as over the Arctic and the Himalayas) can be  
100 considerably large.

101 The TP is surrounded by various sources of pollutants. Over the South of TP, previous  
102 studies have suggested that South Asia was the main source of pollutants transported to the  
103 plateau (e.g., Cong et al., 2009, 2015a, b; Kopacz et al., 2011; Lu et al., 2012; Zhao et al., 2013;  
104 Wang et al., 2015; Zhang et al., 2015; Kang et al., 2016, 2019; Li et al., 2016; Chen et al.,  
105 2018). A huge blanket or layer of “haze” composes of light-absorbing carbonaceous aerosol

106 particles that often erupts in the pre-monsoon season over South Asia and has a significant  
107 influence on the plateau (e.g., Prasad and Singh, 2007; Engling and Gelencser, 2010). Among  
108 them, biomass burning emission reaching the maximum in pre-monsoon season over South  
109 Asia is one of the dominant sources (e.g., Cong et al., 2015b). Many studies investigated the  
110 transport mechanisms of South Asian pollutants to the TP and found that the pollutants  
111 transported across the Himalayas were mainly due to the combination of large-scale circulation  
112 and regional wind (e.g., Hindman and Upadhyay, 2002; Cao et al., 2010; Dumka et al., 2010;  
113 Marinoni et al., 2010; Cong et al., 2015a; Kang et al., 2016; Lüthi et al., 2015; Zhang et al.,  
114 2017). Cong et al. (2015b) suggested that strong large-scale westerly and local small-scale  
115 mountain-valley wind passed through western Nepal, northwest India and Pakistan (i.e.,  
116 southern Himalayas) in the pre-monsoon season. Dumka et al. (2010) and Kang et al. (2016)  
117 inferred from the trajectory analysis that long-distance transport from Africa and Europe may  
118 also affect the BC concentration of Himalayas in addition to the influence of regional pollution.  
119 The synoptic troughs and ridges were also found favoring the transport of pollutants into the  
120 TP from South Asia (Lüthi et al., 2015).

121 Although previous studies have confirmed the transport of pollutants across the Himalayas,  
122 the complex topography of Himalayas complicates transport mechanisms. On one hand, Cao  
123 et al. (2010) revealed that the Himalayas acted as a huge barrier to the transport of a large  
124 amount of BC over the plateau based on model simulations. On the other hand, some studies  
125 found that the valleys across the Himalayas served as channels for efficient transport of  
126 pollutants (e.g., Hindman and Upadhyay, 2002; Marinoni et al., 2010). Marinoni et al. (2010)  
127 analyzed the observation of wind at a station of the southern Himalayas and found that a distinct  
128 valley wind system with the prominent southerly continuously transported pollutants to the  
129 plateau. Most of these studies used observations and back-trajectory models to demonstrate the  
130 transport pathways of pollutants to the TP, which cannot explicitly reveal the transport  
131 mechanisms underneath, in particular quantifying the impacts of complex topography.

132 A few of modeling studies investigated the pollutant transport mechanisms using 3-D  
133 chemical transport models (e.g., Kopacz et al., 2011; Liu et al., 2015; Zhang et al., 2017; Yang  
134 et al., 2018). However, most of them simulated transport processes at relatively coarse  
135 horizontal resolutions (e.g., 20-100 km), which cannot resolve well the complex topography of  
136 Himalayas. It is noteworthy that studies about the aerosol climatic impact over the TP also used  
137 climate models at relatively coarse horizontal resolutions (e.g., Flanner and Zender, 2005;  
138 Menon et al., 2010; Kopacz et al., 2011; Qian et al., 2011, 2015; He et al., 2014; Zhang et al.,  
139 2015; Ji et al., 2016). So far, there is only one study that used a chemical transport model at a

140 horizontal resolution of sub-10 km to investigate pollutant transport mechanisms over the  
141 eastern Himalayas (Cao et al., 2010). Furthermore, none of studies assessed quantitatively the  
142 impacts of topography on modeling the pollutant transport across the Himalayas and hence on  
143 estimating aerosol distribution and radiative forcing over the TP.

144 In order to examine the potential impacts of complex topography on pollutant transport  
145 across the Himalayas over the TP, this study conducts multiple experiments with the Weather  
146 Research and Forecasting Model coupled with chemistry (WRF-Chem, Grell et al., 2005;  
147 Skamarock et al., 2008). The WRF-Chem model is selected because it includes the interaction  
148 between meteorology and aerosol and is widely used for regional modeling of aerosol and its  
149 climatic impact (e.g., Cao et al., 2010; Zhao et al., 2010, 2011, 2012, 2014; Wu et al., 2013;  
150 Gao et al., 2014; Huang et al., 2015; Fan et al., 2015; Feng et al., 2016; Zhong et al., 2017;  
151 Sarangi et al., 2019; Liu et al., 2020). The model has also been used to investigate the aerosol  
152 transport and climatic impact over the Himalayas region (e.g., Feng et al., 2016; Cao et al.,  
153 2010; Sarangi et al., 2019). The model is suitable for simulations at hydrostatic and non-  
154 hydrostatic scales and thus can be used for investigating the impacts of resolution-dependent  
155 feature, such as topography, on modeling results. In particular, the meteorological part of the  
156 model (WRF) has been systematically evaluated and used to investigate the impacts of  
157 resolutions on simulations of moisture transport and climate over the Himalayas region (e.g.,  
158 Shi et al., 2008; Karki et al., 2017; Lin et al., 2018; Zhou et al., 2017, 2018; Wang et al., 2020).  
159 All of these previous studies with the model lay the foundation for this modeling study.

160 Two experiments with different topography representations are conducted to investigate  
161 the impacts of topography complexity on the pollutant transport across the Himalayas and the  
162 resulting radiative forcing over the TP. The simulations are conducted for April 2016 in pre-  
163 monsoon season, because South Asia is seriously polluted during this period and the pollutants  
164 transported to the TP during the period may have significant impacts on Asian monsoon system  
165 (e.g., Lau et al., 2006a, b; Ding et al., 2009; Kuhlmann and Quaas, 2010; Qian et al., 2011,  
166 2015). In addition, the observed concentration of BC at the observation station besides Mt.  
167 Everest shows an evident pollution episode from April 5<sup>th</sup> to 16<sup>th</sup> of 2016, deserving the  
168 investigation of the transport mechanisms. The rest of the paper is organized as follows. Section  
169 2 describes briefly the WRF-Chem model, the physics parameterizations, and the model  
170 configuration for this study, followed by a description of data for evaluation. The series of  
171 numerical experiments at different resolutions are analyzed in Section 3. The findings are then  
172 summarized and discussed in Section 4 and 5.

173

## 174 **2. Methodology**

### 175 **2.1 Model and experiments**

#### 176 2.1.1 WRF-Chem model

177 In this study, the version of WRF-Chem updated by University of Science and Technology  
178 of China (USTC version of WRF-Chem) is used. This USTC version of WRF-Chem includes  
179 some additional capabilities such as the diagnosis of radiative forcing of aerosol species, land  
180 surface coupled biogenic volatile organic compound (VOC) emission, aerosol-snow  
181 interaction compared with the publicly released version (Zhao et al., 2013a, b, 2014, 2016; Hu  
182 et al., 2019; Du et al., 2020). The Model for Simulating Aerosol Interactions and Chemistry  
183 (MOSIAC) (Zaveri et al., 2008) and the Carbon Bond Mechanism-Z (CBM-Z) gas phase  
184 mechanisms (Zaveri and Peters, 1999) are selected. The MOSAIC aerosol scheme uses an  
185 approach of segmentation to represent aerosol size distribution with four or eight discrete size  
186 bins (Fast et al., 2006). It consists of a range of physical and chemical processes such as  
187 nucleation, condensation, coagulation, aqueous phase chemistry, and water uptake by aerosol.  
188 The parameterization of dry deposition of aerosol mass and number is according to the method  
189 of Binkowski and Shankar (1995), including particle diffusion and gravitational effects.  
190 Aerosol-cloud interactions were included in the model by Gustafson et al. (2007) for  
191 calculating the activation and re-suspension between dry aerosols and cloud droplets. The wet  
192 removal of grid-resolved stratiform clouds/precipitation includes two aspects, namely in-cloud  
193 removal (rainout) and below-cloud removal (washout) by Easter et al. (2004) and Chapman et  
194 al. (2009), respectively. Aerosol optical properties such as single scattering albedo (SSA) and  
195 scattering asymmetry and so on are calculated at each model grid through the function of  
196 wavelength. The shortwave (SW) and longwave (LW) refractive indices of aerosols use the  
197 Optical Properties of Aerosols and Clouds (OPAC) data set (Hess et al., 1998), with a detailed  
198 description of the computation of aerosol optical properties can be found in Barnard et al. (2010)  
199 and Zhao et al. (2013a). For both short wave and long wave radiation, aerosol radiation  
200 feedback combined with the Rapid Radiative Transfer Model (RRTMG) (Mlawer et al., 1997;  
201 Iacono et al., 2000) was implemented by Zhao et al. (2011). For the diagnosis of the optical  
202 properties and direct radiative forcing of various aerosol species in the atmosphere, the method  
203 described by Zhao et al (2013a) is adopted. The radiative forcing of light absorbing aerosol in  
204 surface snow is estimated with the Snow, Ice, and Aerosol Radiative model (SNICAR)  
205 (Flanner and Zender, 2005) in the land surface scheme as introduced by Zhao et al. (2014).

206 More details about the coupling between the WRF-Chem and SNICAR models can be found  
207 in Zhao et al. (2014).

208

### 209 2.1.2 Numerical experiments

210 In this study, the WRF-Chem simulations are performed with two nested domains (one-  
211 way nesting), one outer domain at 20-km horizontal resolution with 350×250 grid cells (62°E  
212 -112°E, 1°N -38°N) and one inner domain at 4-km horizontal resolution with 400×300 grid  
213 cells (75°E -92°E, 23°N -35°N) (Fig. 1). The inner domain roughly covers the entire Himalayas.  
214 The WRF-Chem simulations conducted in this study use the terrain following coordinate  
215 (Skamarock et al., 2008). To resolve the vertical structure of transport across the Himalayas,  
216 the simulations are configured with 54 vertical layers and denser layers near the surface. For  
217 example, averaged over a region (26°N-28°N, 76°E-80°E) near the southern Himalayas, there  
218 are about 17 layers below 2 km above the ground (Fig. 2). The goal of this study is to investigate  
219 the impacts of different representations of topography on the transport of BC across the  
220 Himalayas. Therefore, besides this control experiment, one sensitivity (idealized) experiment  
221 is also conducted with the same configuration as the control one except that the terrain heights  
222 of the inner domain at 4-km resolution are bilinearly interpolated from the terrain heights at  
223 20-km resolution similar as previous studies (e.g., Shi et al., 2008; Wu et al., 2012b; Lin et al.,  
224 2018). The two experiments are referred to the simulations with complex and smooth  
225 topography, respectively, hereafter.

226 Fig. 3 shows the spatial distribution of terrain height over the inner domain with complex  
227 (4-km dataset) and smooth (20-km dataset) topography. It is evident that the terrain is much  
228 smoother from the 20-km dataset than from the 4-km dataset. The mountain ridges and valleys  
229 can be resolved to some extent in the 4-km dataset but mostly missed or underestimated at 20-  
230 km. The probability distributions of terrain height from the 20-km and 4-km datasets (Fig. S1  
231 in the supporting material) show that the difference between the two datasets is small for the  
232 terrain height lower than ~4.5 km but is significant for the terrain height above ~4.5 km. In  
233 addition, the slopes between the neighboring grids are significantly reduced in general with the  
234 smooth topography compared to with the complex topography, particularly over the Himalayas  
235 region (Fig. S2 in the supporting material). The difference of results from the two experiments  
236 over the inner domain is analyzed as the impacts of topography representations. Therefore, all  
237 the results shown below are from the simulations of the inner domain at 4-km resolution with  
238 different topography if not otherwise stated. It is noteworthy that this study focuses on

239 understanding the impact of complex topography resolved by 4 km instead of the difference  
240 between 4-km and 20-km simulations. Prescribing the topography at 4 km following the 20-  
241 km resolution distribution is just one way to smooth the topography. In fact, the sensitivity  
242 experiment at 4-km resolution with the topography from the one-degree resolution dataset is  
243 also conducted, and the result is consistent. In addition, although the topography at 4-km  
244 resolution resolves much better topography of Himalayas than that at 20-km resolution, it still  
245 cannot fully resolve the complexity of topography of Himalayas. The higher resolution (e.g., 1  
246 km or sub-1 km) may be needed. Previous studies have found that the simulations at the  
247 resolutions between 1 km and 4 km can produce generally consistent features, but the  
248 simulation at 1 km with better representation of topography can produce a little better  
249 meteorological field compared to the observations (e.g., Karki et al., 2017). One sensitivity  
250 experiment at 1.5-km resolution is also conducted in this study and found the difference  
251 between the simulations at 1.5-km and 4-km resolutions is relatively small. However, it should  
252 be noted that the simulation at 1.5-km resolution is only conducted covering a much smaller  
253 region for a shorter period due to the computational cost. The experiment at 4-km instead of  
254 1.5-km resolution is conducted finally for the study region and period due to the balance of  
255 resolving the complex topography to some extent and affordable computational cost.

256 The simulations are conducted for March 29th-April 20 of 2016 for the reason as discussed  
257 in the introduction. The results of April 1<sup>th</sup>-20<sup>th</sup> are analyzed for the observed pollution episode  
258 to allow a few days spin-up for chemical initial condition. The meteorological initial and lateral  
259 boundary conditions are derived from the European Centre for Medium-Range Weather  
260 Forecasts (ECMWF) reanalysis data at  $0.5^{\circ} \times 0.66^{\circ}$  horizontal resolution and 6 h temporal  
261 intervals (ERA-Interim dataset). The modeled u and v component wind, atmospheric  
262 temperature, and geopotential height over the outer domain are nudged towards the reanalysis  
263 data with a nudging timescale of 6 h following previous studies (e.g., Stauffer and Seaman,  
264 1990; Seaman et al., 1995; Liu et al., 2012; Zhao et al., 2014; Karki et al., 2017; Hu et al., 2016,  
265 2020). Spectral nudging method is applied to balance the performance of simulation at the large  
266 and small scales (Liu et al., 2012), and only to the layers above the planetary boundary layer  
267 (PBL) with nudging coefficients of  $3 \times 10^{-4} \text{ s}^{-1}$ . A wave number of three is selected for both  
268 south-north and west-east directions. Please note that the choices of nudging coefficients and  
269 wave numbers for spectral nudging in this study are empirical. The purpose of nudging is to  
270 simulate reasonably large-scale feature so that small-scale impacts from the complex  
271 topography can be focused. Therefore, the modeling sensitivity to these choices is not tested in



272 this study. The results show that the simulations with nudging method can reproduce the large-  
273 scale circulation at 700 hPa and higher over the outer domain compared to the reanalysis dataset  
274 with the spatial correlation coefficient of 0.96-0.98.

275 The Mellor-Yamada-Nakanishi-Niino (MYNN) planetary boundary layer scheme  
276 (Nakanishi and Niino, 2006), Community Land Model (CLM) land surface scheme (Oleson et  
277 al., 2010), Morrison 2-moment microphysics scheme (Morrison et al., 2009), Kain-Fritsch  
278 cumulus scheme (Kain, 2004), and Rapid Radiative Transfer Model (RRTMG) longwave and  
279 shortwave radiation schemes (Iacono et al., 2000) are used in this study. The chemical initial  
280 and boundary conditions are provided by a quasi-global WRF-Chem simulation for the same  
281 time period to include long-range transported chemical species. The quasi-global WRF-Chem  
282 simulation is performed at  $1^{\circ}\times 1^{\circ}$  horizontal resolution using a quasi-global channel  
283 configuration with  $360\times 130$  grid cells ( $180^{\circ}\text{W}-180^{\circ}\text{E}$ ,  $60^{\circ}\text{S}-70^{\circ}\text{N}$ ). More details about the  
284 general configuration of quasi-global WRF-Chem simulation can be found in Zhao et al.  
285 (2013b) and Hu et al. (2016). The detailed configuration of WRF-Chem experiments is  
286 summarized in Table 1. Due to the lack of publicly available in-situ observations, this study  
287 does not tend to evaluate systematically the simulated meteorological fields over the Himalayas  
288 region. However, as shown in Table 1, the choice of physical parameterizations in this study  
289 follows that of one previous study (Karki et al., 2017) that evaluated systematically the WRF  
290 simulation for one entire year over the Himalayas region. Their results showed that the WRF  
291 simulation at convection-permitting scale could generally capture the essential features of  
292 meteorological fields such as precipitation, temperature, and wind over the Himalayas region.  
293 Therefore, the WRF-Chem simulations in this study are reliable to investigate the impacts of  
294 topography over the Himalayas region.

295

### 296 2.1.3 Emissions

297 Anthropogenic emissions for outer and inner simulation domains are obtained from the  
298 Hemispheric Transport of Air Pollution version-2 (HTAPv2) at  $0.1^{\circ}\times 0.1^{\circ}$  horizontal resolution  
299 and a monthly temporal resolution for year 2010 (Janssens-Maenhout et al., 2015), except that  
300 emissions of East Asia are from the MIX Asian anthropogenic emission inventory at  $0.1^{\circ}\times 0.1^{\circ}$   
301 horizontal resolution for 2015 (Li et al., 2017). Biomass burning emissions are obtained from  
302 the Fire Inventory from National Center for Atmospheric Research (FINN) with hourly  
303 temporal resolution and 1-km horizontal resolution (Wiedinmyer et al., 2011) for the  
304 simulation period, and are vertically distributed following the injection heights suggested by

305 Dentener et al. (2006) from the Aerosol Comparison between Observations and Models  
306 (AeroCom) project. Sea-salt emission follows Zhao et al. (2013b), which includes correction  
307 of particles with radius less than  $0.2 \mu\text{m}$  (Gong, 2003) and dependence of sea-salt emission on  
308 sea surface temperature (Jaeglé et al., 2011). The vertical dust fluxes are calculated with the  
309 Georgia Tech/Goddard Global Ozone Chemistry Aerosol Radiation and Transport (GOCART)  
310 dust emission scheme (Ginoux et al., 2001), and the emitted dust particles are distributed into  
311 the MOSAIC aerosol size bins following a theoretical expression based on the physics of scale-  
312 invariant fragmentation of brittle materials derived by Kok (2011). More details about the dust  
313 emission scheme coupled with MOSAIC aerosol scheme in WRF-Chem can be found in Zhao  
314 et al. (2010, 2013b).

315 As shown in Fig. 1, anthropogenic fossil fuel emissions of BC are high over Northeast  
316 India. The fossil fuel BC emissions over Nepal, the country nearby the southern Himalayas,  
317 are relatively low. Instead, biomass burning emissions of BC are extremely high in Nepal and  
318 Northwest India (South Himalayas,  $26^{\circ}\text{N}$ - $29^{\circ}\text{N}$ ). Averaged over the South Himalayas of inner  
319 domain that may significantly affect the pollutant transport into the TP, the biomass burning  
320 emissions of BC are much higher than its anthropogenic fossil fuel emissions, particularly for  
321 the pollution episode (Fig. 4). The anthropogenic BC emissions are set constant through April,  
322 while biomass burning emissions show a strong fire event in April 5-16. During the event, the  
323 biomass burning BC emissions can be a factor of 2 of the anthropogenic fossil fuel BC  
324 emissions over South Himalayas.

325

## 326 **2.2 Dataset**

327 Three datasets are used to compare with the modeling results to demonstrate the pollutant  
328 episode and spatial distribution. One is from the Moderate Resolution Imaging  
329 Spectroradiometer (MODIS) instruments on Aqua and Terra satellites. The MODIS Aerosol  
330 Product monitors the ambient aerosol optical thickness over the oceans globally and over the  
331 continents. Daily Level 2 Aerosol Optical Depth (AOD) at 550 nm products with the spatial  
332 resolution of  $10 \text{ km} \times 10 \text{ km}$  (at nadir) from both Aqua and Terra are applied. When compared  
333 with the modeling results, the simulations are sampled at the satellite overpass time and  
334 location. The second one is from the Aerosol Robotic Network (AERONET) (Holben et al.,  
335 1998) that has  $\sim 100$  similar globally distributed sun and sky scanning ground-based automated  
336 radiometers, which provide measurements of aerosol optical properties throughout the world  
337 (Dubovik and King, 2000; Dubovik et al., 2002). In this study, AERONET measured AOD at  
338 675 nm and 440 nm from two sites over the TP, QOMS\_CAS site ( $86.95^{\circ}\text{E}$ ,  $28.36^{\circ}\text{N}$ ) and

339 NAM\_CO site (90.96°E, 30.77°N) are used to derive the AOD at 550 nm (using the Angström  
340 exponent) for comparison with modeling results at 550 nm. All of the retrievals of AOD are at  
341 quality level 2, and the uncertainty of AOD measurements is about 0.01 (Holben et al., 2001).  
342 In this study, the available data in April 2016 are used to evaluate the modeling results during  
343 the same period.

344 The third one is the measurement of near-surface BC mass concentration collected during  
345 the simulation period for April 4-20 of 2016 at the Qomolangma Station for Atmospheric and  
346 Environmental Observation and Research (QOMS, 86.95°E, 28.36°N) which is located at the  
347 northern slope of the Mt. Everest, about 4276 meters above sea level. The BC mass  
348 concentration is measured with the widely-used instrument Aethalometer (AE-33) that can  
349 provide real-time BC mass concentration measurements. The calibration of air flow is routinely  
350 conducted to maintain the data quality. The instrument estimates the BC mass concentration  
351 based on the optical method through measuring the reduction in light intensity induced by BC.  
352 The method assumes that the relationship between attenuation and BC surface loading is linear  
353 for low attenuation values. However, this relationship becomes nonlinear when the attenuation  
354 values are high due to a filter saturation effect, which may lead to underestimation of the high  
355 BC concentration. The detection limit of AE-33 instrument is 5 ng/m<sup>3</sup>, and the uncertainty is  
356 estimated to be within 10% (e.g., Chen et al., 2018; Bansal et al., 2019; Kant et al., 2019). The  
357 dataset of BC mass concentration used in this study was reported by Chen et al., (2018), where  
358 more details about the measurements can be found.

359

### 360 **3. Results**

#### 361 **3.1 Spatial distribution of BC around the TP**

362 Figure 5 shows the spatial distributions of column integrated BC mass within the inner  
363 domain from the simulations at 4-km resolution with complex and smooth topography  
364 averaged for April 1-20, 2016, and the difference between the two is also shown. For both  
365 experiments, the Himalayas is an apparent boundary line for the distribution of BC with a sharp  
366 gradient across the Himalayas. The high BC mass loading exists near the southern Himalayas  
367 reaching over 10 mg/m<sup>2</sup>, which is largely contributed by the biomass burning emissions during  
368 the period (Fig. 4), while the value reduces significantly to less than 0.4 mg/m<sup>2</sup> over the TP.  
369 The BC mass loading near the central and eastern Himalayas is higher than that near the  
370 western Himalayas. In general, the column BC mass loading from the simulation with complex  
371 topography is higher over the TP and lower over the region to the south of Himalayas compared

372 with the smooth topography, reflecting the stronger transport of BC from the source region to  
373 the Himalayas and TP due to the complex topography (see the discussion in Section 3.2). Figure  
374 6 displays the spatial distributions of AOD from the MODIS retrievals and the simulations at  
375 4 km with two different topography averaged for April 1-20, 2016. In general, both simulations  
376 reproduce the overall spatial distribution of AOD, with the large values near the southern  
377 Himalayas, consistent with the BC mass loading. In addition, both the simulations and satellite  
378 retrievals show higher AOD near the central and eastern Himalayas than that near the western  
379 Himalayas during the study period. The difference between the simulations and retrievals may  
380 be partly related to the uncertainties in emissions particularly for biomass burning emissions.  
381 Other than intense emissions, the wind circulation around the TP may also play an important  
382 role in accumulating BC near the southern Himalayas. Because of the block of Himalayas, the  
383 wind circulation at 500 hPa is divided into two branches as westerly and northwesterly. Both  
384 of them are relatively dry airflows with little effect on pollutant removal, favor the  
385 accumulation of pollutants near the southern Himalayas, and carry the pollutants to the TP (e.g.,  
386 Dumka et al., 2010; Kang et al., 2016; Cong et al., 2015a).

387 The AOD retrieved at two AERONET sites over the TP are compared with the two  
388 simulations for April 1-20, 2016 (Fig. 7). The AOD at the QOMS\_CAS site near the northern  
389 Himalayas is higher than that at the NAM\_CO site inside of the TP. Both simulations can  
390 capture this gradient. The simulation with complex topography produces higher AOD than  
391 does the one with smooth topography at both sites. The modeling biases (normalized mean bias,  
392 NMB) reduce from -46% (smooth topography) to 9% (complex topography) at the  
393 QOMS\_CAS site and from -26% (smooth topography) to -10% (complex topography) at the  
394 NAM\_CO site. Although the correlation coefficient between the simulations and observation  
395 increases from 0.37 (smooth topography) to 0.53 (complex topography) at the QOMS\_CAS  
396 site, it is similar (~0.2) between the two simulations at the NAM\_CO site. The correlation  
397 coefficient is higher at the QOMS\_CAS site near the source region than the NAM\_CO site  
398 farther away, which may indicate the model processes affecting the transport over the TP still  
399 need examination with more observations. The NAM\_CO site over the eastern TP may also be  
400 affected by other sources that are not counted in this study. The modeling of temporal variations  
401 of pollutants over the TP deserves further investigation with more observations.

402 There is one in-situ observational station (QOMS) near the Mt. Everest (black dot shown  
403 in Fig. 1) to collect the near-surface BC concentration. The observed near-surface BC  
404 concentration at this station is compared with the corresponding simulations for this period as  
405 shown in Figure 8. Without local emission source, the near-surface BC concentration at QOMS

406 is primarily contributed by the transport. The temporal variation of observed near-surface BC  
407 concentration correlates highly with the biomass burning emissions as shown in Fig. 4, with  
408 the peak value on April 11 reaching  $\sim 3 \text{ ug/m}^3$ . One sensitivity experiment without biomass  
409 burning emissions shows that the simulated BC concentration at QOMS will be significantly  
410 reduced without the peak (not shown), which further proves that the BC concentration over the  
411 northern Himalayas can be largely influenced by the pollution episode near the southern  
412 Himalayas. It is noteworthy that both simulations can reproduce the episode in time and  
413 magnitude, and the difference at this station is small. The spatial distribution of difference in  
414 near-surface BC concentration between the two simulations (Fig. S3) is more heterogeneous  
415 than that of column BC mass (Fig. 5), reflecting the impact of topography on near-surface  
416 transport (see the discussion in Section 3.2).

417

### 418 **3.2 Transport flux into the TP**

419 To further understand the difference in BC surface concentration and column mass loading  
420 over the TP between the two simulations with different topography, Figure 9 shows the  
421 longitude-height cross section of BC transport flux along the cross line (shown as the black  
422 dash line in Fig. 3) from the two simulations at local time (LT) 03:00 and 15:00 averaged for  
423 April 1-20 to represent nighttime and daytime transport, respectively. The PBL height along  
424 the cross line is also shown as the black dash line. The transport flux is calculated by projecting  
425 the wind field perpendicularly to the cross line and then multiplying the BC mass concentration  
426 along the cross line. More specifically, the transport flux is calculated as following:

$$427 \quad \text{TF} = C * (u * \sin \alpha + v * \sin \beta) \quad (1)$$

428 Where  $\alpha$  is the angle between east-west wind component and the cross line,  $\beta$  is the angle  
429 between south-north wind component and the cross line, and  $C$  is the BC mass concentration  
430 at the grid along the cross line. The flux is estimated at each model level. Positive values  
431 represent the transport towards the TP, while negative values represent the transport away from  
432 the TP. It is evident that BC is imported into the TP during the day and night on the west of  
433  $\sim 85^\circ\text{E}$ , although the transport flux is much larger during the daytime than nighttime. On the  
434 east of  $\sim 85^\circ\text{E}$ , BC is imported into the TP during the day but exported slightly from the TP  
435 during the night. The difference of transport flux between the western and eastern Himalayas  
436 is primarily due to the influence of large-scale westerly that is weak over the eastern Himalayas  
437 (Fig. 5). The transport across the western Himalayas is controlled by the large-scale westerly,  
438 while local southerly dominates the transport across the eastern Himalayas and also influences

439 the transport across the central Himalayas (Fig. S4 in the supporting material). The stronger  
440 diurnal variation of local southerly (towards the TP in the daytime to away from the TP in the  
441 nighttime) than that of westerly near the surface (Fig. S4) leads to the large difference in diurnal  
442 variation of transport between the western and eastern Himalayas. The strong transport is  
443 primarily within the PBL during the daytime, and the deeper PBL during the daytime allows  
444 BC over the source region mixed to higher altitude, which also leads to stronger import  
445 transport during the day than the night. The relatively small difference in simulated PBL  
446 heights and structure between the two experiments can be due to their different surface heating  
447 resulted from different topography complexity (e.g., Wagner et al., 2014).

448 The difference between the simulations with two different topography is evident. The  
449 mountain ridges are much higher and valleys are much deeper with the complex topography  
450 than with the smooth topography. The simulation with smooth topography produces  
451 overwhelming crossing-Himalayas transport towards the TP within the PBL, in particular  
452 during the daytime. Although, in the simulation with complex topography, the mountain ridges  
453 resolved weaken the crossing-Himalayas transport compared to the simulation with smooth  
454 topography, the overall positive values near the surface indicate that the transport can overcome  
455 most mountain ridges along the Himalayas. The transport fluxes near the surface from the  
456 simulation with complex topography become close-to-zero only at a few mountain ridges that  
457 are 6.5 km or higher. To better demonstrate the transport pathway across mountain ridges, one  
458 cross-section across the mountain ridge as shown as one black solid line in Fig. 3 is taken as  
459 one example. Figure 10 shows the latitude-height cross section of BC mass concentration and  
460 transport flux across one mountain ridge from the simulations with complex and smooth  
461 topography at local time (LT) 03:00 and 15:00 averaged for April 1-20, 2016. Near the southern  
462 part of mountain, the elevated concentration of BC mass accumulates and can mix up reaching  
463 as high as 5 km with the much stronger transport during the daytime. It is obvious that the  
464 mountain ridge in the simulation with smooth topography is quite low. With the high mountain  
465 ridge resolved by the complex topography, the simulated BC transport flux can still cross the  
466 mountain. Analysis of transport flux across a few more mountain ridges indicates similar  
467 results (not shown). The results above indicate that the transport of pollutants can cross a  
468 majority of mountain ridges of Himalayas, which is consistent with the observation-based  
469 estimate by Gong et al. (2019) that also found pollutants could overcome the blocking effect  
470 of mountain ridges of Himalayas as a transport pathway. On the other hand, the resolved deeper  
471 valleys in the simulation with complex topography enhance the transport flux compared to the  
472 one with the smooth topography. Similarly, Figure 11 shows one example of latitude-height

473 cross section of BC mass concentration and transport flux across one valley from the  
474 simulations with complex and smooth topography at local time (LT) 03:00 and 15:00 averaged  
475 for April 1-20, 2016. The transport is much stronger and deeper along the valley from the  
476 simulation with complex topography than the one with smooth topography. Again, analysis of  
477 transport flux across a few more valleys does not show different results (not shown).

478 In order to further demonstrate the overall inflow flux across the Himalayas, the vertically  
479 integrated BC mass flux along the longitudinal cross section (as shown in Fig. 9) from the  
480 simulations with different topography is shown in Figure 12. The terrain heights from the two  
481 simulations along the cross section are also shown as black lines. The total mass flux is  
482 calculated by integrating the right-hand term of equation (1) as following:

$$483 \quad \text{ITF} = \int_{z=z_{sc}}^{z=z_{top}} \delta z * C * (u * \sin \alpha + v * \sin \beta) \quad (2)$$

484 Where  $\delta z$  is the thickness of each vertical model level. Similarly, positive values represent  
485 the transport towards the TP, while negative values represent the transport away from the TP.  
486 More evidently, the positive BC inflows towards the TP occur not only through the valleys but  
487 also across the mountain ridges with both topography. The negative values only exist to the  
488 east of 88°E. With complex topography, higher mountain ridges can reduce the transport flux  
489 to some extent compared to the smooth topography. The complex topography results in  
490 significantly larger BC inflow towards the TP compared to the smooth topography, particularly  
491 corresponding to the deep valleys, such as the Karnali River Valley around 82°E and the Kali  
492 Gandaki Valley around 84°E.

493 One reason for the enhanced transport across the Himalayas with the complex topography  
494 is the resolved deeper valleys that lead to the increased valley wind. The wind across some  
495 valleys can be significantly larger with the complex topography than the smooth one (Fig. S4).  
496 The enhanced valley wind across the Himalayas has also been found by previous studies with  
497 observations and numerical simulations (e.g., Egger et al., 2000; Zängl et al., 2001; Carrera et  
498 al., 2009; Karki et al., 2017; Lin et al., 2018). However, it is noteworthy that previous studies  
499 have found that the orographic drag (including gravity wave drag and turbulence orographic  
500 form drag) over the region with complex topography, such as the Himalayas and other  
501 mountainous areas, would weaken the overall near-surface wind speed (e.g., Beljaars et al.,  
502 2004; Horvath et al., 2012; Jiménez and Dudhia, 2012; Zhou et al., 2017, 2018; Lin et al., 2018;  
503 Wang et al, 2020). Therefore, the near-surface wind speed is also examined. The complex  
504 topography does lead to the overall reduction of near-surface wind speed over the Himalayas  
505 area (Fig. S5 in the supporting material), which is consistent with previous studies. However,

506 it is interesting to note that the near-surface southerly wind during the daytime of the simulation  
507 period is overall increased over the Himalayas area with the complex topography (Fig. 13),  
508 which indicates that the transport towards the TP is strengthened with the complex topography  
509 in the daytime, particularly over the central and eastern Himalayas where the BC mass loading  
510 is higher (Fig. 5). During the night, the meridional wind is dominated by northerly over the  
511 Himalayas region in the simulation with the smooth topography. The complex topography  
512 weakens the transport away from the TP or change the wind direction from northerly to  
513 southerly over some areas of Himalayas. Both effects enhance the overall transport efficiency  
514 across the Himalayas towards the TP. Therefore, although the complex topography weakens  
515 the overall near-surface wind speed around the Himalayas, it induces more realistic small-scale  
516 mountain-valley circulation that favors the BC transport across the Himalayas towards TP  
517 during the study period. Another effect of resolving valleys is that the volume of relatively-  
518 high-concentration BC could be higher with deeper valleys (Fig. S6 in the support material),  
519 which can also result in stronger transport towards the TP even if the wind condition is similar.  
520 For example, the altitude (above the ground) below which the BC mass concentration is larger  
521 than  $0.3/\mu\text{g m}^3$  is much higher along the valleys with the complex topography than with the  
522 smooth topography (Fig. S7 in the support material). The correlation coefficient between the  
523 difference of terrain heights of valleys and of volumes of relatively-high-concentration BC can  
524 reach -0.76, indicating that the lower the valleys are, the higher the volumes of BC mass can  
525 be transported across the Himalayas. The combined influence of these factors results in  
526 significantly enhanced BC transport towards the TP with the complex topography (Fig. 12),  
527 which can also be demonstrated by the distributions of wind and BC mass concentration along  
528 the longitudinal cross section (Fig. S8a, b in the support material).

529 The enhanced transport across the Himalayas turns out that the overall BC inflow with the  
530 complex topography is much stronger than that with the smooth topography. Figure 14 shows  
531 the accumulated integrated total transport flux of BC across the Himalayas estimated from the  
532 simulations with complex and smooth topography for April 1-20, 2016. The accumulated  
533 import flux of BC increases during the period in both experiments, and the difference between  
534 the two experiments gradually increases with the time. At the end of period, the simulation  
535 with complex topography estimates a total import flux of BC of  $\sim 1.5 \times 10^4$  Ton that is  $\sim 50\%$   
536 higher than  $\sim 1.0 \times 10^4$  Ton estimated based on the simulation with smooth topography. The  
537 sensitivity analysis by moving the cross line (cross-section of the analysis in Fig. 9, 12, 14)



538 towards or away from the TP within a certain distance and re-calculating the flux indicates that  
539 the impacts of topography on the simulated results do not change significantly.

540 All the analysis above focuses on investigating the BC transport flux across the Himalayas.  
541 Although the inflow can reflect the impact of transport on the BC mass over the TP to some  
542 extent, the change of BC mass concentration is eventually determined by the convergence of  
543 transport. Therefore, the contribution of each model process (transport, dry-deposition,  
544 emission, PBL mixing, and wet deposition) to the increase of BC column mass averaged over  
545 the TP (with elevation > 4 km) during this episode is analyzed for both simulations following  
546 the methodology introduced by Du et al. (2020). The results show that the two main processes  
547 affecting the BC column mass over the TP during the period are transport and dry deposition.  
548 The transport is the dominant process that increases the BC column mass over the TP, while  
549 the dry deposition reduces it. The contribution of transport to the increase of BC column mass  
550 over the TP during the episode from the simulation with complex topography is significantly  
551 larger than that with the smooth topography, which is consistent with the results shown by  
552 analyzing the transport flux across the Himalayas. Although the impacts of PBL mixing and  
553 wet deposition on the BC column mass over the TP are also different between the simulations  
554 with different topography, their impacts are much smaller than those of transport and dry  
555 deposition during the study period.

556

### 557 **3.3 Radiative forcing of BC over the TP**

558 The BC transported over the TP could significantly influence the regional climate and  
559 water resources over Asia through heating the atmosphere and accelerating the melting of snow  
560 and glacier (e.g., Qian et al., 2011, 2015; Lau et al., 2017). Therefore, the impact of the complex  
561 topography on estimating the BC radiative heating profile in the atmosphere and radiative  
562 forcing in surface snow deserves investigation. Figure 15 shows the vertical profiles of BC  
563 induced radiative heating rate in the atmosphere averaged over the TP (with elevation > 4 km)  
564 within the inner domain shown in Fig.1 for April 1-20, 2016 from the simulations with complex  
565 and smooth topography. Both simulations generate higher BC heating rate near the surface and  
566 the rate gradually decreases with altitude, which is consistent with the vertical profiles of BC  
567 mass concentration averaged over the TP (Fig. S9 in the supporting material). The BC heating  
568 rate over the TP from the simulation with complex topography is ~0.17 K/day near the surface  
569 and reduces to ~0.08 K/day at 8 km, which is ~50% and ~30%, respectively, higher than that  
570 from the simulation with smooth topography at the corresponding altitudes. The higher BC

571 heating rate over the TP estimated by the simulation with complex topography is consistent  
572 with its higher BC column mass (Fig. 5) and concentration profile (Fig. S9).

573 The BC radiative forcing in surface snow is controlled by both the distributions of BC  
574 mass concentration and snow coverage (e.g., Zhao et al., 2014). Figure 16 shows the spatial  
575 distributions of snow water equivalent (SWE) averaged for April 1-20, 2016 from the  
576 simulations with two topography. The difference between the two is also shown. It shows that  
577 the simulation with complex topography generates more areas with higher SWE compared to  
578 that with the smooth topography over the TP. Along the Himalayas, the simulated SWE is  
579 higher over the mountain ridges with the complex topography, particularly for the East  
580 Himalayas, while the smooth topography leads to broader snow coverage over the West  
581 Himalayas. The difference in SWE between the two simulations is highly correlated with their  
582 difference in precipitation (Fig. S10 in the supporting material). Along the Himalayas, the  
583 simulated precipitation with the complex topography is larger than that with the smooth  
584 topography at the mountain ridges and smaller at the valleys. Over the TP, the overall  
585 precipitation is larger with the complex topography than that with the smooth topography (Fig.  
586 S10). Previous studies have found that the topography could significantly affect the  
587 precipitation over the Himalayas region (e.g., Bookhagen and Burbank, 2010; Wulf et al., 2016;  
588 Cannon et al., 2017; Karki et al., 2017).

589 Figure 17 shows the spatial distributions of BC radiative forcing in the surface snow over  
590 the TP averaged for April 1-20, 2016 from the simulations with two topography, and the  
591 difference between the two is also shown. The BC radiative forcing in surface snow is largely  
592 coincident with the spatial distributions of SWE as shown in Fig. 16, mainly due to the  
593 heterogeneous distributions of snow cover over the TP. The BC radiative forcing in surface  
594 snow over the TP from the simulation with complex topography reaches  $5 \text{ W/m}^2$  where the  
595 snow exists, larger than that with the smooth topography. Along the Himalayas, the simulation  
596 with complex topography produces higher BC snow forcing over the mountain ridges,  
597 particularly over the eastern Himalayas, while the one with the smooth topography simulates  
598 higher BC snow forcing over most areas of western Himalayas due to its broader snow  
599 coverage there. Overall, the complex topography leads to higher BC forcing in snow over the  
600 TP and the eastern Himalayas and lower BC forcing in snow over the western Himalayas, and  
601 therefore results in the different distribution of BC forcing in snow over the TP and Himalayas,  
602 compared to that with the smooth topography.

603  
604

605

#### 606 **4. Summary**

607 In this study, the model experiments with different topography are conducted to illustrate  
608 the impacts of complexity of topography of Himalayas on BC transport from South Asia to the  
609 TP. The observed pollution episode at the QOMS station besides the Mt. Everest during the  
610 pre-monsoon season is simulated. The observed near-surface BC concentration shows a peak  
611 of  $\sim 3 \text{ ug/m}^3$  much larger than the background value of  $< 0.4 \text{ ug/m}^3$  over the TP. The observed  
612 temporal variation of near-surface BC concentrations correlates highly with that of biomass  
613 burning emissions near the southern Himalayas, indicating the significant impacts of biomass  
614 burning on the pollutants over the TP. The simulations can reproduce the episode in time and  
615 magnitude, and are used to investigate the BC transport mechanisms and the impacts of  
616 topography.

617 The high BC mass loading during the simulation period accumulates near the southern  
618 Himalayas driven by the large-scale westerly and small-scale southerly circulations, which is  
619 also observed by satellites. The modeling results demonstrate that the circulations favor the  
620 accumulation of pollutants near the Himalayas, particularly the central and eastern parts, and  
621 can carry the pollutants to the TP during the study period, which is consistent with previous  
622 modeling studies (e.g., Kopacz et al., 2011). It is noteworthy that the BC accumulated near the  
623 southern Himalayas can be transported across the Himalayas overcoming a majority of  
624 mountain ridges, which is consistent with the observation-based estimate by Gong et al. (2019)  
625 that also found pollutants could overcome the blocking effect of the mountain ridges of  
626 Himalayas. However, the transport through the valleys is found much stronger and more  
627 efficient than across the mountain ridges and the enhancement effect cannot be ignored. The  
628 complex topography results in 50% higher overall transport flux across the Himalayas during  
629 the simulation period than that with the smooth topography, primarily due to the strengthened  
630 efficiency of near-surface meridional transport towards the TP, enhanced wind speed at some  
631 valleys, and deeper valley channels associated with larger BC mass volume that can be  
632 transported into the TP, although the overall wind speed is weakened due to the orographic  
633 drags with the complex topography. This turns out that the simulation with complex  
634 topography produces 30-50% higher BC radiative heating rate in the atmosphere up to 10 km  
635 averaged over the TP than does the simulation with smooth topography.

636 For the BC radiative forcing in surface snow, the simulation with complex topography  
637 produces stronger forcing over the TP than that with the smooth one. The complex topography

638 makes the distribution of BC forcing in surface snow quite different from the simulation with  
639 smooth topography, partly due to its different distribution of surface snow. The simulated BC  
640 radiative forcing in snow is distributed more heterogeneously than those in previous studies  
641 using global models at relatively coarse resolutions (e.g., Qian et al., 2011). He et al. (2014)  
642 used a global chemical transport model to simulate the BC forcing in snow at the horizontal  
643 resolution of  $\sim 0.2^\circ$  and obtained the similar distribution as the simulation with smooth  
644 topography in this study with the high values over the western Himalayas. However, their  
645 simulated values near the Himalayas are higher than the simulated results of this study, which  
646 may be due to their estimation are averaged for November-April.

647 This study highlights the importance of resolving complex topography of the Himalayas  
648 in modeling the aerosol transport across the Himalayas and radiative impact over the TP.  
649 Although this study focuses on the impacts of topography on the simulated results, the  
650 additional analysis (Fig. S11-13 in the supporting material) of the outer domain simulation at  
651 20-km resolution and the inner domain simulation at 4 km with different topography indicates  
652 that the resolution-dependent difference between 20 km and 4 km is largely contributed by  
653 their different representations of topography over the Himalayas region, consistent with  
654 previous studies (e.g., Karki et al., 2017; Lin et al., 2018). Climate models at coarser horizontal  
655 resolutions than 20 km and thus with relatively smooth topography may underestimate the  
656 aerosol transport from South Asia to the TP during the pre-monsoon season and represent  
657 inappropriately the aerosol radiative forcing in the atmosphere and surface snow over the TP.

658

## 659 **5. Discussion**

660 Previous studies also found the induced change of circulation and transport due to the  
661 complex topography at convection-permitting scales with the focus on the meteorological  
662 fields over the Himalayas and TP regions (e.g., Karki et al., 2017; Zhou et al., 2017, 2018; Lin  
663 et al., 2018; Wang et al., 2020). Most of them either conducted the sub-10 km simulations  
664 covering a relatively smaller region (e.g.,  $101 \times 96$  grids at 5 km in Karki et al., 2017;  $181 \times 121$   
665 grids at 2 km in Lin et al., 2018;  $\sim 330 \times 230$  grids at 3 km in Wang et al., 2020) compared to  
666 this study ( $400 \times 300$  grids at 4 km) or conducted the simulations covering the entire Himalayas  
667 but at the resolutions above 10 km and with the sub-grid orographic drag parameterization to  
668 consider the impact of complex topography. Although some of previous studies also showed  
669 that the resolved complex topography yielded more realistic small-scale mountain-valley  
670 circulations and enhanced valley winds over the Himalayas region compared to the smoother

671 topography, the overall moisture transport across the Himalayas towards the TP was weaker  
672 with the complex topography due to the orographic drags.

673 The difference between previous studies and this study can be due to several factors. First,  
674 previous studies focused on moisture instead of air pollutants. The spatial (horizontal and  
675 vertical) distributions between air pollutants and moisture are different and may contribute to  
676 the different impacts of topography on the overall transport flux across the Himalayas.  
677 However, the analysis of the moisture from the simulations in this study shows the increase of  
678 moisture transport (not shown) and hence the increase of precipitation over the TP with the  
679 complex topography (Fig. S10). Second, most of previous studies focused on monsoon season  
680 instead of pre-monsoon season. Therefore, the meteorological simulations for monsoon season  
681 (June-July-August) at different resolutions are also conducted in this study. The results show  
682 that the moisture transport and precipitation are reduced at the higher resolution with complex  
683 topography and the meridional wind is overall weakened particularly over the central and  
684 eastern Himalayas and TP (not shown), which is consistent with previous studies. This may  
685 indicate that the different large-scale circulations between the two seasons (much stronger  
686 southerly during the monsoon season) may also lead to different impacts of complex  
687 topography on meridional winds and hence cross-Himalayas transport.

688 Since this study only demonstrates the potential impacts for a relatively short period, a  
689 longer-term study should be conducted to examine the impacts of topography on aerosol  
690 climatic effect over the TP in both pre-monsoon and monsoon seasons. In addition, the active  
691 convection during the monsoon season may also play an important role on pollutant transport  
692 across the Himalayas, which deserves further investigation. Furthermore, aerosol impact on  
693 cloud and precipitation, particularly during the monsoon season, and thus on the latent heat in  
694 the atmosphere and the associated responses may also depend on the complex topography.  
695 Previous studies based on observations found that the rain frequency and intensity reached the  
696 highest and the cloud thickness reached the deepest at the foothill of Himalayas and decreased  
697 as the elevation increased up to the TP (e.g., Chen et al., 2017; Fu et al., 2018; Zhang et al.,  
698 2018), which was explained by Fu et al. (2018) due to the blocking of the air flow by the steep  
699 slope of southern Himalayas. However, the large amount of transported aerosol along the slope  
700 from the foothill up to the TP may also play a role. These potential impacts of aerosols on  
701 regional hydro-climate around the TP and over Asia using high-resolution model that can  
702 resolve the complex topography of Himalayas and TP deserve further investigation.

703

704 **Data availability**

705 The released version of WRF-Chem can be downloaded from  
706 [http://www2.mmm.ucar.edu/wrf/users/download/get\\_source.html](http://www2.mmm.ucar.edu/wrf/users/download/get_source.html). The updated USTC  
707 version of WRF-Chem can be downloaded from <http://aemol.ustc.edu.cn/product/list/> or  
708 contact [chunzhao@ustc.edu.cn](mailto:chunzhao@ustc.edu.cn). Also, the code modifications will be incorporated the release  
709 version of WRF-Chem in future.

710

711 **Author contributions**

712 Meixin Zhang and Chun Zhao designed the experiments, conducted and analyzed the  
713 simulations. All authors contributed to the discussion and final version of the paper.

714

715 **Acknowledgements**

716 This research was supported by the National Key Research and Development Program of  
717 China (2016YFA0602001), the National Natural Science Foundation of China NSFC (Grant  
718 No. 91837310), the second Tibetan Plateau Scientific Expedition and Research Program (STEP)  
719 (2019QZKK0605), and the Fundamental Research Funds for the Central Universities. The  
720 study used computing resources from the High-Performance Computing Center of University  
721 of Science and Technology of China (USTC) and the TH-2 of National Supercomputer Center  
722 in Guangzhou (NSCC-GZ).

723

724 **Reference**

- 729 Bansal, O., Singh, A., and Singh, D.: Characteristics of Black Carbon aerosols over Patiala  
730 Northwestern part of the IGP: Source apportionment using cluster and CWT analysis,  
731 Atmospheric Pollution Research, 10, 244–256, doi:10.1016/j.apr.2018.08.001, 2019.
- 732 Barnard, J. C., Fast, J. D., Paredes-Miranda, G., Arnott, W. P., and Laskin, A.: Technical Note:  
733 Evaluation of the WRF-Chem "Aerosol Chemical to Aerosol Optical Properties" Module  
734 using data from the MILAGRO campaign, Atmos. Chem. Phys., 10, 7325–7340,  
735 doi:10.5194/acp-10-7325-2010, 2010.
- 736 Beljaars, A. C., Brown, A. R., and Wood, N.: A new parametrization of turbulent orographic  
737 form drag, QJ Roy. Meteorol. Soc., 130, 1327–1347, doi: 10.1256/qj.03.73, 2004.
- 738 Barnett, T. P., Adam, J. C., and Lettenmaier, D. P.: Potential impacts of a warming climate on  
739 water availability in snow-dominated regions, Nature, 438, 303–309,  
740 doi:10.1038/nature04141, 2005.
- 741 Binkowski, F. S. and Shankar, U.: The Regional Particulate Matter Model: 1. Model  
742 description and preliminary results, J. Geophys. Res., 100, 26191, doi:10.1029/95JD02093,  
743 1995.
- 744 Bookhagen, B. and Burbank, D. W.: Toward a complete Himalayan hydrological budget:  
745 Spatiotemporal distribution of snowmelt and rainfall and their impact on river discharge, J.  
746 Geophys. Res., 115, 39, doi:10.1029/2009JF001426, 2010.
- 747 Boos, W. R. and Kuang, Z.: Sensitivity of the South Asian monsoon to elevated and non-  
748 elevated heating, Scientific reports, 3, 1192, doi:10.1038/srep01192, 2013.
- 749 Cannon, F., Carvalho, L. M. V., Jones, C., Norris, J., Bookhagen, B., and Kiladis, G. N.: Effects  
750 of topographic smoothing on the simulation of winter precipitation in High Mountain Asia,  
751 J. Geophys. Res. Atmos., 122, 1456–1474, doi:10.1002/2016JD026038, 2017.
- 752 Cao, J., Tie, X., Xu, B., Zhao, Z., Zhu, C., Li, G., and Liu, S.: Measuring and modeling black  
753 carbon (BC) contamination in the SE Tibetan Plateau, Journal of Atmospheric Chemistry,  
754 67, 45–60, doi:10.1007/s10874-011-9202-5, 2010.
- 755 Carrera, M. L., Gyakum, J. R., and Lin, C. A.: Observational Study of Wind Channeling within  
756 the St. Lawrence River Valley, J. Appl. Meteorol. Clim., 48, 2341–2361,  
757 doi:10.1175/2009JAMC2061.1, 2009.
- 758 Chapman, E. G., Gustafson, W. I., Easter, R. C., Barnard, J. C., Ghan, S. J., Pekour, M. S., and  
759 Fast, J. D.: Coupling aerosol-cloud-radiative processes in the WRF-Chem model:

760 Investigating the radiative impact of elevated point sources, *Atmos. Chem. Phys.*, 9, 945–  
761 964, doi:10.5194/acp-9-945-2009, 2009.

762 Chen, J. and Bordoni, S.: Orographic Effects of the Tibetan Plateau on the East Asian Summer  
763 Monsoon: An Energetic Perspective, *J. Climate*, 27, 3052–3072, doi:10.1175/JCLI-D-13-  
764 00479.1, 2014.

765 Chen, X., Kang, S., Cong, Z., Yang, J., and Ma, Y.: Concentration, temporal variation, and  
766 sources of black carbon in the Mt. Everest region retrieved by real-time observation and  
767 simulation, *Atmos. Chem. Phys.*, 18, 12859–12875, doi:10.5194/acp-18-12859-2018, 2018.

768 Chen, Y., Fu, Y., Xian, T., and Pan, X.: Characteristics of cloud cluster over the steep southern  
769 slopes of the Himalayas observed by CloudSat, *Int. J. Climatol.*, 37, 4043–4052,  
770 doi:10.1002/joc.4992, 2017.

771 Cong, Z., Kang, S., and Qin, D.: Seasonal features of aerosol particles recorded in snow from  
772 Mt. Qomolangma (Everest) and their environmental implications, *Journal of environmental  
773 sciences (China)*, 21, 914–919, doi:10.1016/S1001-0742(08)62361-X, 2009.

774 Cong, Z., Kang, S., Kawamura, K., Liu, B., Wan, X., Wang, Z., Gao, S., and Fu, P.:  
775 Carbonaceous aerosols on the south edge of the Tibetan Plateau: concentrations, seasonality  
776 and sources, *Atmos. Chem. Phys.*, 15, 1573–1584, doi:10.5194/acp-15-1573-2015, 2015a.

777 Cong, Z., Kawamura, K., Kang, S., and Fu, P.: Penetration of biomass-burning emissions from  
778 South Asia through the Himalayas: new insights from atmospheric organic acids, *Scientific  
779 reports*, 5, 9580, doi:10.1038/srep09580, 2015b.

780 Dentener, F., Kinne, S., Bond, T., Boucher, O., Cofala, J., Generoso, S., Ginoux, P., Gong, S.,  
781 Hoelzemann, J. J., Ito, A., Marelli, L., Penner, J. E., Putaud, J. P., Textor, C., Schulz, M.,  
782 van der Werf, G. R., and Wilson, J.: Emissions of primary aerosol and precursor gases in the  
783 years 2000 and 1750, prescribed data-sets for AeroCom, *Atmos. Chem. Phys.*, 6, 4321–4344,  
784 doi:10.5194/acp-6-4321-2006, 2006.

785 Ding, Y., Sun, Y., Wang, Z., Zhu, Y., and Song, Y.: Inter-decadal variation of the summer  
786 precipitation in China and its association with decreasing Asian summer monsoon Part II:  
787 Possible causes, *Int. J. Climatol.*, 29, 1926–1944, doi:10.1002/joc.1759, 2009.

788 Du, Q., Zhao, C., Zhang, M., Dong, X., Chen, Y., Liu, Z., Hu, Z., Zhang, Q., Li, Y., Yuan, R.,  
789 , and Miao, S.: Modelling diurnal variation of surface PM<sub>2.5</sub> concentration over East China  
790 with WRF-Chem: Impacts from boundary layer mixing and anthropogenic  
791 emission, *Atmos. Chem. Phys. Discuss.*, [https://doi.org/10.5194/acp-2019-](https://doi.org/10.5194/acp-2019-739)  
792 739, in review, 2020.



793 Duan, A. M. and Wu, G. X.: Role of the Tibetan Plateau thermal forcing in the summer climate  
794 patterns over subtropical Asia, *Climate Dynamics*, 24, 793–807, doi:10.1007/s00382-004-  
795 0488-8, 2005.

796 Dubovik, O. and King, M. D.: A flexible inversion algorithm for retrieval of aerosol optical  
797 properties from Sun and sky radiance measurements, *J. Geophys. Res.*, 105, 20673–20696,  
798 doi:10.1029/2000JD900282, 2000.

799 Dubovik, O., Holben, B., Eck, T. F., Smirnov, A., Kaufman, Y. J., King, M. D., Tanré, D., and  
800 Slutsker, I.: Variability of Absorption and Optical Properties of Key Aerosol Types  
801 Observed in Worldwide Locations, *J. Atmos. Sci.*, 59, 590–608, doi:10.1175/1520-  
802 0469(2002)059<0590:VOAAOP>2.0.CO;2, 2002.

803 Dumka, U. C., Moorthy, K. K., Kumar, R., Hegde, P., Sagar, R., Pant, P., Singh, N., and Babu,  
804 S. S.: Characteristics of aerosol black carbon mass concentration over a high altitude location  
805 in the Central Himalayas from multi-year measurements, *Atmospheric Research*, 96, 510–  
806 521, doi:10.1016/j.atmosres.2009.12.010, 2010.

807 Easter, R. C., Ghan, S. J., Zhang, Y., Saylor, R. D., Chapman, E. G., Laulainen, N. S., Abdul-  
808 Razzak, H., Leung, L. R., Bian, X., and Zaveri, R. A.: MIRAGE: Model Description and  
809 Evaluation of Aerosols and Trace Gases, *J. Geophys. Res.*, 109, D20210,  
810 doi:10.1029/2004JD004571, 2004.

811 Egger, J., Bajracharya, S., Egger, U., Heinrich, R., Reuder, J., Shakya, P., Wendt, H., and Wirth,  
812 V.: Diurnal winds in the Himalayan Kali Gandaki Valley. Part I: Observations, *Mon.*  
813 *Weather Rev.*, 128, 1106–1122, 2000.

814 Engling, G. and Gelencser, A.: Atmospheric Brown Clouds: From Local Air Pollution to  
815 Climate Change, *Elements*, 6, 223–228, doi:10.2113/gselements.6.4.223, 2010.

816 Fan, J., Rosenfeld, D., Yang, Y., Zhao, C., Leung, L. R., and Li, Z.: Substantial contribution  
817 of anthropogenic air pollution to catastrophic floods in Southwest China, *Geophys. Res. Lett.*,  
818 42, 6066–6075, doi:10.1002/2015GL064479, 2015.

819 Fast, J. D., Gustafson Jr, W. I., Easter, R. C., Zaveri, R. A., Barnard, J. C., Chapman, E. G.,  
820 Grell, G. A., and Peckham, S. E.: Evolution of ozone, particulates, and aerosol direct  
821 radiative forcing in the vicinity of Houston using a fully coupled meteorology-chemistry-  
822 aerosol model, *J. Geophys. Res.*, 111, D21305, doi:10.1029/2005JD006721, 2006.

823 Feng, Y., Kotamarthi, V. R., Coulter, R., Zhao, C., and Cadeddu, M.: Radiative and  
824 thermodynamic responses to aerosol extinction profiles during the pre-monsoon month over  
825 South Asia, *Atmos. Chem. Phys.*, 16, 247–264, doi:10.5194/acp-16-247-2016, 2016.

826 Flanner, M. G. and Zender, C. S.: Snowpack radiative heating: Influence on Tibetan Plateau  
827 climate, *Geophys. Res. Lett.*, 32, L06501, doi:10.1029/2004GL022076, 2005.

828 Fu, Y., Pan, X., Xian, T., Liu, G., Zhong, L., Liu, Q., Li, R., Wang, Y., and Ma, M.:  
829 Precipitation characteristics over the steep slope of the Himalayas in rainy season observed  
830 by TRMM PR and VIRS, *Climate dynamics*, 51, 1971-1989, doi: 10.1007/s00382-017-  
831 3992-3, 2018.

832 Gao, Y., Zhao, C., Liu, X., Zhang, M., and Leung, L. R.: WRF-Chem simulations of aerosols  
833 and anthropogenic aerosol radiative forcing in East Asia, *Atmospheric Environment*, 92,  
834 250–266, doi:10.1016/j.atmosenv.2014.04.038, 2014.

835 Ginoux, P., Chin, M., Tegen, I., Prospero, J. M., Holben, B., Dubovik, O., and Lin, S.-J.:  
836 Sources and distributions of dust aerosols simulated with the GOCART model, *J. Geophys.*  
837 *Res.*, 106, 20255–20273, doi:10.1029/2000JD000053, 2001.

838 Gong, P., Wang, X., Pokhrel, B., Wang, H., Liu, X., Liu, X., and Wania, F.: Trans-Himalayan  
839 Transport of Organochlorine Compounds: Three-Year Observations and Model-Based Flux  
840 Estimation, *Environ. Sci. Technol.*, 53, 6773–6783, doi:10.1021/acs.est.9b01223, 2019.

841 Gong, S. L.: A parameterization of sea-salt aerosol source function for sub- and super-micron  
842 particles, *Global Biogeochem. Cycles*, 17, n/a-n/a, doi:10.1029/2003GB002079, 2003.

843 Grell, G. A., Peckham, S. E., Schmitz, R., McKeen, S. A., Frost, G., Skamarock, W. C., and  
844 Eder, B.: Fully coupled “online” chemistry within the WRF model, *Atmospheric*  
845 *Environment*, 39, 6957–6975, doi:10.1016/j.atmosenv.2005.04.027, 2005.

846 Gustafson, W. I., E. G. Chapman, S. J. Ghan, R. C. Easter, and J. D. Fast: Impact on modeled  
847 cloud characteristics due to simplified treatment of uniform cloud condensation nuclei  
848 during NEAQS 2004, *Geophys. Res. Lett.*, 34, L19809, doi:10.1029/2007GL030021, 2007.

849 Hansen, J. and Nazarenko, L.: Soot climate forcing via snow and ice albedos, *Proceedings of*  
850 *the National Academy of Sciences*, 101, 423–428, doi:10.1073/pnas.2237157100, 2004.

851 He, C., Li, Q., Liou, K. N., Takano, Y., Gu, Y., Qi, L., Mao, Y., and Leung, L. R.: Black carbon  
852 radiative forcing over the Tibetan Plateau, *Geophys. Res. Lett.*, 41, 7806–7813,  
853 doi:10.1002/2014GL062191, 2014.

854 He, C., Wang, Z., Zhou, T., and Li, T.: Enhanced Latent Heating over the Tibetan Plateau as a  
855 Key to the Enhanced East Asian Summer Monsoon Circulation under a Warming Climate,  
856 *J. Climate*, 32, 3373–3388, doi:10.1175/JCLI-D-18-0427.1, 2019.

857 Hess, M., Koepke, P., and Schult, I.: Optical Properties of Aerosols and Clouds: The Software  
858 Package OPAC, *Bull. Amer. Meteor. Soc.*, 79, 831–844, doi:10.1175/1520-  
859 0477(1998)079<0831:OPOAAC>2.0.CO;2, 1998.

860 Hindman, E. E. and Upadhyay, B. P.: Air pollution transport in the Himalayas of Nepal and  
861 Tibet during the 1995–1996 dry season, *Atmospheric Environment*, 36, 727–739,  
862 doi:10.1016/S1352-2310(01)00495-2, 2002.

863 Holben, B. N., Eck, T. F., Slutsker, I., Tanré, D., Buis, J. P., Setzer, A., Vermote, E., Reagan,  
864 J. A., Kaufman, Y. J., Nakajima, T., Lavenu, F., Jankowiak, I., and Smirnov, A.:  
865 AERONET—A Federated Instrument Network and Data Archive for Aerosol  
866 Characterization, *Remote Sensing of Environment*, 66, 1–16, doi:10.1016/S0034-  
867 4257(98)00031-5, 1998.

868 Holben, B. N., Tanre, D., Smirnov, A., ECK T. F., Slutsker, I., Abuhassan, N., Newcomb, W.,  
869 Schafer, J., Chatenet, B., Lavenu, F., Kaufman, Y., Vande Castle, J., Setzer, A., Markham,  
870 B., Clark, D., Frouin, R., Halthore, R., Karneli, A., O'Neill, N., Pietras, C., Pinker, R., Voss,  
871 K., and Zibordi, G.: An emerging ground-based aerosol climatology: Aerosol optical depth  
872 from AERONET, *J. Geophys. Res.*, 106, 12067-12097, doi:10.1029/2001JD900014, 2001.

875 Horvath, K., Koracin, D., Vellore, R., Jiang, J., and Belu, R.: Sub - kilometer dynamical  
876 downscaling of near - surface winds in complex terrain using WRF and MM5 mesoscale  
877 models, *J. Geophys. Res. Atmos.*, 117, D11111, doi:10.1029/2012JD017432, 2012

878 Hu, Z., Huang, J., Zhao, C., Bi, J., Jin, Q., Qian, Y., Leung, L. R., Feng, T., Chen, S., and Ma,  
879 J.: Modeling the contributions of Northern Hemisphere dust sources to dust outflow from  
880 East Asia, *Atmospheric Environment*, 202, 234–243, doi:10.1016/j.atmosenv.2019.01.022,  
881 2019.

882 Hu, Z., Huang, J., Zhao, C., Jin, Q., Ma, Y., and Yang, B.: Modeling dust sources, transport,  
883 and radiative effects at different altitudes over the Tibetan Plateau, *Atmos. Chem. Phys.*  
884 *Discuss.*, <https://doi.org/10.5194/acp-2019-431>, in press, 2020.

885 Hu, Z., Zhao, C., Huang, J., Leung, L. R., Qian, Y., Yu, H., Huang, L., and Kalashnikova, O.V.:  
886 Trans-pacific transport and evolution of aerosols: Evaluation of quasi global WRF-Chem  
887 simulation with multiple observations, *Geosci. Model Dev.*, 9, 1725–1746, doi:10.5194/  
888 gmd-9-1725-2016, 2016.

889 Huang, X., Song, Y., Zhao, C., Cai, X., Zhang, H., and Zhu, T.: Direct Radiative Effect by  
890 Multicomponent Aerosol over China, *J. Climate*, 28, 3472–3495, doi:10.1175/JCLI-D-14-  
891 00365.1, 2015.

892 Iacono, M. J., Mlawer, E. J., Clough, S. A., and Morcrette, J. J.: Impact of an improved  
893 longwave radiation model, RRTM, on the energy budget and thermodynamic properties of

894 the NCAR community climate model, CCM3, *J. Geophys. Res.*, 105, 14873–14890,  
895 doi:10.1029/2000JD900091, 2000.

896 Immerzeel, W. W., van Beek, L. P. H., and Bierkens, M. F. P.: Climate change will affect the  
897 Asian water towers, *Science* (New York, N.Y.), 328, 1382–1385,  
898 doi:10.1126/science.1183188, 2010.

899 Jaeglé, L., Quinn, P. K., Bates, T. S., Alexander, B., and Lin, J. T.: Global distribution of sea  
900 salt aerosols: new constraints from in situ and remote sensing observations, *Atmos. Chem.*  
901 *Phys.*, 11, 3137–3157, doi:10.5194/acp-11-3137-2011, 2011.

902 Janssens-Maenhout, G., Crippa, M., Guizzardi, D., Dentener, F., Muntean, M., Pouliot, G.,  
903 Keating, T., Zhang, Q., Kurokawa, J., Wankmüller, R., van der Denier Gon, H., Kuenen, J.  
904 J. P., Klimont, Z., Frost, G., Darras, S., Koffi, B., and Li, M.: HTAP\_v2.2: a mosaic of  
905 regional and global emission grid maps for 2008 and 2010 to study hemispheric transport of  
906 air pollution, *Atmos. Chem. Phys.*, 15, 11411–11432, doi:10.5194/acp-15-11411-2015,  
907 2015.

908 Ji, Z. M.: Modeling black carbon and its potential radiative effects over the Tibetan Plateau,  
909 *Advances in Climate Change Research*, 7, 139–144, doi:10.1016/j.accre.2016.10.002, 2016.

910 Ji, Z., Kang, S., Cong, Z., Zhang, Q., and Yao, T.: Simulation of carbonaceous aerosols over  
911 the Third Pole and adjacent regions: distribution, transportation, deposition, and climatic  
912 effects, *Clim Dyn*, 45, 2831–2846, doi:10.1007/s00382-015-2509-1, 2015.

913 Jiménez, P. A. and Dudhia, J.: Improving the representation of resolved and unresolved  
914 topographic effects on surface wind in the WRF model, *J. Appl. Meteorol. Clim.*, 51, 300-  
915 316, doi:10.1175/JAMC-D-11-084.1, 2012.

916 Kain, J. S.: The Kain–Fritsch Convective Parameterization: An Update, *J. Appl. Meteor.*, 43,  
917 170–181, doi:10.1175/1520-0450(2004)043<0170:TKCPAU>2.0.CO;2, 2004.

918 Kang, S, Chen P, Li C, Liu B, Cong Z: Atmospheric Aerosol Elements over the Inland Tibetan  
919 Plateau: Concentration, Seasonality, and Transport, *Aerosol Air Qual. Res.*, 16, 789–800,  
920 doi:10.4209/aaqr.2015.02.0307, 2016.

921 Kang, S., Q. Zhang, Y. Qian, Z. Ji, C. Li, Z. Cong, Y. Zhang, J. Guo, W. Du, J. Huang, Q. You,  
922 A. K. Panday, M. Rupakheti, D. Chen, O. Gustafsson, M. H. Thiemens, and D. Qin: Linking  
923 atmospheric pollution to cryospheric change in the Third Pole region: current progress and  
924 future prospects, *National Science Review*, 6, 796–809, doi:10.1093/nsr/nwz031, 2019.

925 Kant, Y., Shaik, D. S., Mitra, D., Chandola, H. C., Babu, S. S., and Chauhan, P.: Black carbon  
926 aerosol quantification over north-west Himalayas: Seasonal heterogeneity, source

927 apportionment and radiative forcing, *Environmental pollution* (Barking, Essex 1987),  
928 113446, doi:10.1016/j.envpol.2019.113446, 2019.

929 Karki, R., ul Hasson, S., Gerlitz, L., Schickhoff, U., Scholten, T., and Böhner, J.: Quantifying  
930 the added value of convection-permitting climate simulations in complex terrain: a  
931 systematic evaluation of WRF over the Himalayas, *Earth Syst. Dynam.*, 8, 507–528,  
932 doi:10.5194/esd-8-507-2017, 2017.

933 Kok, J. F.: A scaling theory for the size distribution of emitted dust aerosols suggests climate  
934 models underestimate the size of the global dust cycle, *Proceedings of the National Academy  
935 of Sciences of the United States of America*, 108, 1016–1021, doi:10.1073/pnas.1014798108,  
936 2011.

937 Kopacz, M., Mauzerall, D. L., Wang, J., Leibensperger, E. M., Henze, D. K., and Singh, K.:  
938 Origin and radiative forcing of black carbon transported to the Himalayas and Tibetan  
939 Plateau, *Atmos. Chem. Phys.*, 11, 2837–2852, doi:10.5194/acp-11-2837-2011, 2011.

940 Kuhlmann, J. and Quaas, J.: How can aerosols affect the Asian summer monsoon? Assessment  
941 during three consecutive pre-monsoon seasons from CALIPSO satellite data, *Atmos. Chem.  
942 Phys.*, 10, 4673–4688, doi:10.5194/acp-10-4673-2010, 2010.

943 Lau, K. M. and Kim, K. M.: Observational relationships between aerosol and Asian monsoon  
944 rainfall, and circulation, *Geophys. Res. Lett.*, 33, D22101, doi: 10.1029/2006GL027546,  
945 2006b.

946 Lau, K. M., Kim, M. K., and Kim, K. M.: Asian summer monsoon anomalies induced by  
947 aerosol direct forcing: the role of the Tibetan Plateau, *Clim Dyn*, 26, 855–864, doi:  
948 10.1007/s00382-006-0114-z, 2006a.

949 Lau, W. K. and Kim, K. M.: Impact of Snow Darkening by Deposition of Light-Absorbing  
950 Aerosols on Snow Cover in the Himalayas–Tibetan Plateau and Influence on the Asian  
951 Summer Monsoon: A Possible Mechanism for the Blanford Hypothesis, *Atmosphere*, 9, 438,  
952 doi:10.3390/atmos9110438, 2018.

953 Lau, W. K. M., Kim, K. M., Shi, J. J., Matsui, T., Chin, M., Tan, Q., Peters-Lidard, C., and  
954 Tao, W. K.: Impacts of aerosol–monsoon interaction on rainfall and circulation over  
955 Northern India and the Himalaya Foothills, *Clim Dyn*, 49, 1945–1960, doi:10.1007/s00382-  
956 016-3430-y, 2017.

957 Lau, W. K. M., Kim, M. K., Kim, K. M., and Lee, W. S.: Enhanced surface warming and  
958 accelerated snow melt in the Himalayas and Tibetan Plateau induced by absorbing aerosols,  
959 *Environ. Res. Lett.*, 5, 25204, doi:10.1088/1748-9326/5/2/025204, 2010.

960 Lee, W. S., Bhawar, R. L., Kim, M. K., and Sang, J.: Study of aerosol effect on accelerated  
961 snow melting over the Tibetan Plateau during boreal spring, *Atmospheric Environment*, 75,  
962 113–122, doi:10.1016/j.atmosenv.2013.04.004, 2013.

963 Li, C., Bosch, C., Kang, S., Andersson, A., Chen, P., Zhang, Q., Cong, Z., Chen, B., Qin, D.,  
964 and Gustafsson, Ö.: Sources of black carbon to the Himalayan–Tibetan Plateau glaciers, *Nat*  
965 *Commun*, 7, 4825, doi:10.1038/ncomms12574, 2016.

966 Li, M., Zhang, Q., Kurokawa, J. i., Woo, J. H., He, K., Lu, Z., Ohara, T., Song, Y., Streets, D.  
967 G., Carmichael, G. R., Cheng, Y., Hong, C., Huo, H., Jiang, X., Kang, S., Liu, F., Su, H.,  
968 and Zheng, B.: MIX: a mosaic Asian anthropogenic emission inventory under the  
969 international collaboration framework of the MICS-Asia and HTAP, *Atmos. Chem. Phys.*,  
970 17, 935–963, doi:10.5194/acp-17-935-2017, 2017.

971 Li, R. and Min, Q. L.: Impacts of mineral dust on the vertical structure of precipitation, *J.*  
972 *Geophys. Res.*, 115, 1337, doi:10.1029/2009JD011925, 2010.

973 Li, R., Dong, X., Guo, J., Fu, Y., Zhao, C., Wang, Y., and Min, Q.: The implications of dust  
974 ice nuclei effect on cloud top temperature in a complex mesoscale convective system, *Sci*  
975 *Rep*, 7, 291, doi:10.1038/s41598-017-12681-0, 2017.

976 Li, R., Shao, W., Guo, J., Fu, Y., Wang, Y., Liu, G., Zhou, R., and Li, W.: A Simplified  
977 Algorithm to Estimate Latent Heating Rate Using Vertical Rainfall Profiles Over the Tibetan  
978 Plateau, *J. Geophys. Res. Atmos.*, 124, 942–963, doi:10.1029/2018JD029297, 2019.

979 Lin, C., Chen, D., Yang, K., and Ou, T.: Impact of model resolution on simulating the water  
980 vapor transport through the central Himalayas: implication for models’ wet bias over the  
981 Tibetan Plateau, *Clim Dyn*, 51, 3195–3207, doi:10.1007/s00382-018-4074-x, 2018.

982 Liu, P., Tsimpidi, A. P., Hu, Y., Stone, B., Russell, A. G., and Nenes, A.: Differences between  
983 downscaling with spectral and grid nudging using WRF, *Atmos. Chem. Phys.*, 12, 3601–  
984 3610, doi:10.5194/acp-12-3601-2012, 2012.

985 Liu, Y., Sato, Y., Jia, R., Xie, Y., Huang, J., and Nakajima, T.: Modeling study on the transport  
986 of summer dust and anthropogenic aerosols over the Tibetan Plateau, *Atmos. Chem. Phys.*,  
987 15, 12581–12594, doi:10.5194/acp-15-12581-2015, 2015.

988 Liu, Z., Ming, Y., Zhao, C., Lau, N. C., Guo, J., Bollasina, M., and Yim, S. H. L.: Contribution  
989 of local and remote anthropogenic aerosols to a record-breaking torrential rainfall event in  
990 Guangdong Province, China, *Atmos. Chem. Phys.*, 20, 223–241, doi:10.5194/acp-20-223-  
991 2020, 2020.

992 Lu, Z., Streets, D. G., Zhang, Q., and Wang, S.: A novel back-trajectory analysis of the origin  
 993 of black carbon transported to the Himalayas and Tibetan Plateau during 1996-2010,  
 994 *Geophys. Res. Lett.*, 39, n/a-n/a, doi:10.1029/2011GL049903, 2012.

995 Lüthi, Z. L., Škerlak, B., Kim, S. W., Lauer, A., Mues, A., Rupakheti, M., and Kang, S.:  
 996 Atmospheric brown clouds reach the Tibetan Plateau by crossing the Himalayas, *Atmos.*  
 997 *Chem. Phys.*, 15, 6007–6021, doi:10.5194/acp-15-6007-2015, 2015.

998 Lutz, A. F., Immerzeel, W. W., Shrestha, A. B., and Bierkens, M. F. P.: Consistent increase in  
 999 High Asia's runoff due to increasing glacier melt and precipitation, *Nature Clim Change*, 4,  
 1000 587–592, doi:10.1038/nclimate2237, 2014.

1001 Marinoni, A., Cristofanelli, P., Laj, P., Duchi, R., Calzolari, F., Decesari, S., Sellegri, K.,  
 1002 Vuillermoz, E., Verza, G. P., and Villani, P.: Aerosol mass and black carbon concentrations,  
 1003 a two year record at NCO-P (5079 m, Southern Himalayas), *Atmos. Chem. Phys.*, 10, 8551–  
 1004 8562, doi:10.5194/acp-10-8551-2010, 2010.

1005 Menon, S., Koch, D., Beig, G., Sahu, S., Fasullo, J., and Orlikowski, D.: Black carbon aerosols  
 1006 and the third polar ice cap, *Atmos. Chem. Phys.*, 10, 4559–4571, doi:10.5194/acp-10-4559-  
 1007 2010, 2010.

1008 Ming, J., Xiao, C., Cachier, H., Qin, D., Qin, X., Li, Z., and Pu, J.: Black Carbon (BC) in the  
 1009 snow of glaciers in west China and its potential effects on albedos, *Atmospheric Research*,  
 1010 92, 114–123, doi:10.1016/j.atmosres.2008.09.007, 2009.

1011 Mlawer, E. J., Taubman, S. J., Brown, P. D., Iacono, M. J., and Clough, S. A.: Radiative  
 1012 transfer for inhomogeneous atmospheres: RRTM, a validated correlated-k model for the  
 1013 longwave, *J. Geophys. Res.*, 102, 16663–16682, doi:10.1029/97JD00237, 1997.

1014 Morrison, H., Thompson, G., and Tatarskii, V.: Impact of Cloud Microphysics on the  
 1015 Development of Trailing Stratiform Precipitation in a Simulated Squall Line: Comparison  
 1016 of One- and Two-Moment Schemes, *Mon. Wea. Rev.*, 137, 991–1007,  
 1017 doi:10.1175/2008MWR2556.1, 2009.

1018 Nakanishi, M. and Niino, H.: An Improved Mellor–Yamada Level-3 Model: Its Numerical  
 1019 Stability and Application to a Regional Prediction of Advection Fog, *Boundary-Layer*  
 1020 *Meteorol.*, 119, 397–407, doi:10.1007/s10546-005-9030-8, 2006.

1021 Oleson, K. W., Lawrence, D. M., Bonan, G. B., Flanner, M. G., Kluzek, E., Lawrence, P. J.,  
 1022 Levis, S., Swenson, S. C., Thornton, P. E., Dai, A., Decker, M., Dickinson, R., Feddema, J.,  
 1023 Heald, C. L., Hoffman, F., Lamarque, J. F., Mahowald, N., Niu, G. Y., Qian, T., Randerson,  
 1024 J., Running, S., Sakaguchi, K., Slater, A., Stockli, R., Wang, A., Yang, Z. L., Zeng, X., and  
 1025 Zeng, X.: Technical Description of version 4.0 of the Community Land Model (CLM), Tech.

1026 Rep. NCAR/TN-478+STR, National Center for Atmospheric Research, Boulder, Colorado,  
 1027 USA, 2010.

1028 Prasad, A. K. and Singh, R. P.: Comparison of MISR-MODIS aerosol optical depth over the  
 1029 Indo-Gangetic basin during the winter and summer seasons (2000–2005), *Remote Sensing*  
 1030 *of Environment*, 107, 109–119, doi:10.1016/j.rse.2006.09.026, 2007.

1031 Qian, Y., Flanner, M. G., Leung, L. R., and Wang, W.: Sensitivity studies on the impacts of  
 1032 Tibetan Plateau snowpack pollution on the Asian hydrological cycle and monsoon climate,  
 1033 *Atmos. Chem. Phys.*, 11, 1929–1948, doi:10.5194/acp-11-1929-2011, 2011.

1034 Qian, Y., Yasunari, T. J., Doherty, S. J., Flanner, M. G., Lau, W. K. M., Ming, J., Wang, H.,  
 1035 Wang, M., Warren, S. G., and Zhang, R.: Light-absorbing particles in snow and ice:  
 1036 Measurement and modeling of climatic and hydrological impact, *Adv. Atmos. Sci.*, 32, 64–  
 1037 91, doi:10.1007/s00376-014-0010-0, 2015.

1038 Qiu, J.: China: The third pole, *Nature*, 454, 393–396, doi:10.1038/454393a, 2008.

1039 Ramanathan, V. and Carmichael, G.: Global and regional climate changes due to black carbon,  
 1040 *Nature Geosci*, 1, 221–227, doi:10.1038/ngeo156, 2008.

1041 Ramanathan, V., Ramana, M. V., Roberts, G., Kim, D., Corrigan, C., Chung, C., and Winker,  
 1042 D.: Warming trends in Asia amplified by brown cloud solar absorption, *Nature*, 448, 575–  
 1043 578, doi:10.1038/nature06019, 2007.

1044 Sarangi, C., Qian, Y., Rittger, K., Bormann, K. J., Liu, Y., Wang, H., Lin, G., and Painter, T.  
 1045 H.: Impact of light-absorbing particles on snow albedo darkening and associated radiative  
 1046 forcing over high-mountain Asia: high-resolution WRF-Chem modeling and new satellite  
 1047 observations. *Atmos. Chem. Phys.*, 19, 7105–7128, doi:10.5194/acp-19-7105-2019, 2019.

1048 Seaman, N. L., Stauffer, D. R., and Lario-Gibbs, A. M.: A Multiscale Four-Dimensional Data  
 1049 Assimilation System Applied in the San Joaquin Valley during SARMAP. Part I: Modeling  
 1050 Design and Basic Performance Characteristics, *J. Appl. Meteor.*, 34, 1739–1761,  
 1051 doi:10.1175/1520-0450(1995)034<1739:AMFDDA>2.0.CO;2, 1995.

1052 Shi, X., Wang, Y., and Xu, X.: Effect of mesoscale topography over the Tibetan Plateau on  
 1053 summer precipitation in China: A regional model study, *Geophys. Res. Lett.*, 35, 255,  
 1054 doi:10.1029/2008GL034740, 2008.

1055 Singh, P. and Bengtsson, L.: Hydrological sensitivity of a large Himalayan basin to climate  
 1056 change, *Hydrol. Process.*, 18, 2363–2385, doi:10.1002/hyp.1468, 2004.

1057 Skamarock, W. C., Klemp, J. B., Dudhia, J., Gill, D. O., Barker, D. M., Duda, M., Huang, X.  
 1058 Y., Wang, W., and Powers, J. G.: A Description of the Advanced Research WRF Version 3,



1059 NCAR Technical Note, NCAR/TN-468+STR, available at: <http://wrf->  
1060 [model.org/wrfadmin/docs/arw\\_v2.pdf](http://model.org/wrfadmin/docs/arw_v2.pdf), 2008.

1061 Stauffer, D. R. and Seaman, N. L.: Use of Four-Dimensional Data Assimilation in a Limited-  
1062 Area Mesoscale Model. Part I: Experiments with Synoptic-Scale Data, *Mon. Wea. Rev.*, 118,  
1063 1250–1277, doi:10.1175/1520-0493(1990)118<1250:UOFDDA>2.0.CO;2, 1990.

1064 Wagner, J. S., Gohm, A., and Rotach, M. W.: The Impact of Horizontal Model Grid Resolution  
1065 on the Boundary Layer Structure over an Idealized Valley, *Mon. Wea. Rev.*, 142, 3446–  
1066 3465, doi:10.1175/MWR-D-14-00002.1, 2014.

1067 Wang, X., Gong, P., Sheng, J., Joswiak, D. R., and Yao, T.: Long-range atmospheric transport  
1068 of particulate Polycyclic Aromatic Hydrocarbons and the incursion of aerosols to the  
1069 southeast Tibetan Plateau, *Atmospheric Environment*, 115, 124–131,  
1070 doi:10.1016/j.atmosenv.2015.04.050, 2015.

1071 Wang, Y., Yang, K., Zhou, X., Chen, D., Lu, H., Ouyang, L., Chen, Y., Lazhu., and Wang, B.:  
1072 Synergy of orographic drag parameterization and high resolution greatly reduces biases of  
1073 WRF-simulated precipitation in central Himalaya, *Climate Dynamics*, 54, 1729–1740,  
1074 doi:10.1007/s00382-019-05080-w, 2020.

1075 Wiedinmyer, C., Akagi, S. K., Yokelson, R. J., Emmons, L. K., Al-Saadi, J. A., Orlando, J. J.,  
1076 and Soja, A. J.: The Fire INventory from NCAR (FINN): a high resolution global model to  
1077 estimate the emissions from open burning, *Geosci. Model Dev.*, 4, 625–641,  
1078 doi:10.5194/gmd-4-625-2011, 2011.

1079 Wu, G., Liu, Y., Dong, B., Liang, X., Duan, A., Bao, Q., and Yu, J.: Revisiting Asian monsoon  
1080 formation and change associated with Tibetan Plateau forcing: I. Formation, *Clim Dyn*, 39,  
1081 1169–1181, doi:10.1007/s00382-012-1334-z, 2012a.

1082 Wu, G., Liu, Y., He, B., Bao, Q., Duan, A., and Jin, F. F.: Thermal controls on the Asian  
1083 summer monsoon, *Scientific reports*, 2, 404, doi:10.1038/srep00404, 2012b.

1084 Wu, G., Liu, Y., Zhang, Q., Duan, A., Wang, T., Wan, R., Liu, X., Li, W., Wang, Z., and Liang,  
1085 X.: The Influence of Mechanical and Thermal Forcing by the Tibetan Plateau on Asian  
1086 Climate, *J. Hydrometeor.*, 8, 770–789, doi:10.1175/JHM609.1, 2007.

1087 Wu, L., Su, H., and Jiang, J. H.: Regional simulation of aerosol impacts on precipitation during  
1088 the East Asian summer monsoon, *J. Geophys. Res. Atmos.*, 118, 6454–6467,  
1089 doi:10.1002/jgrd.50527, 2013.

1090 Wulf, H., Bookhagen, B., and Scherler, D.: Differentiating between rain, snow, and glacier  
1091 contributions to river discharge in the western Himalaya using remote-sensing data and

1092 distributed hydrological modeling, *Advances in Water Resources*, 88, 152–169,  
1093 doi:10.1016/j.advwatres.2015.12.004, 2016.

1094 Yang, J., Kang, S., Ji, Z., and Chen, D.: Modeling the Origin of Anthropogenic Black Carbon  
1095 and Its Climatic Effect Over the Tibetan Plateau and Surrounding Regions, *J. Geophys. Res.*  
1096 *Atmos.*, 123, 671–692, doi:10.1002/2017JD027282, 2018.

1097 Yasunari, T. J., Bonasoni, P., Laj, P., Fujita, K., Vuillermoz, E., Marinoni, A., Cristofanelli, P.,  
1098 Duchi, R., Tartari, G., and Lau, K.-M.: Estimated impact of black carbon deposition during  
1099 pre-monsoon season from Nepal Climate Observatory – Pyramid data and snow albedo  
1100 changes over Himalayan glaciers, *Atmos. Chem. Phys.*, 10, 6603–6615, doi:10.5194/acp-  
1101 10-6603-2010, 2010.

1102 Ye, D. Z. and Wu, G. X.: The role of the heat source of the Tibetan Plateau in the general  
1103 circulation, *Meteorol. Atmos. Phys.*, 67, 181–198, doi:10.1007/BF01277509, 1998.

1104 Zängl, G., Egger, J., and Wirth, V.: Diurnal Winds in the Himalayan Kali Gandaki Valley. Part  
1105 II: Modeling, *Mon. Wea. Rev.*, 129, 1062–1080, doi:10.1175/1520-  
1106 0493(2001)129<1062:DWITHK>2.0.CO;2, 2001.

1107 Zaveri, R. A. and Peters, L. K.: A new lumped structure photochemical mechanism for large-  
1108 scale applications, *J. Geophys. Res.*, 104, 30387–30415, doi:10.1029/1999JD900876, 1999.

1109 Zaveri, R. A., Easter, R. C., Fast, J. D., and Peters, L. K.: Model for Simulating Aerosol  
1110 Interactions and Chemistry (MOSAIC), *J. Geophys. Res.*, 113, 1591,  
1111 doi:10.1029/2007JD008782, 2008.

1112 Zhang, A., Fu, Y., Chen, Y., Liu, G., and Zhang, X.: Impact of the surface wind flow on  
1113 precipitation characteristics over the southern Himalayas: GPM observations, *Atmospheric*  
1114 *Research*, 202, 10–22, doi:10.1016/j.atmosres.2017.11.001, 2018.

1115 Zhang, R., Wang, H., Qian, Y., Rasch, P. J., Easter, R. C., Ma, P. L., Singh, B., Huang, J., and  
1116 Fu, Q.: Quantifying sources, transport, deposition, and radiative forcing of black carbon over  
1117 the Himalayas and Tibetan Plateau, *Atmos. Chem. Phys.*, 15, 6205–6223, doi:10.5194/acp-  
1118 15-6205-2015, 2015.

1119 Zhang, R., Wang, Y., He, Q., Chen, L., Zhang, Y., Qu, H., Smeltzer, C., Li, J., Alvarado, L. M.  
1120 A., Vrekoussis, M., Richter, A., Wittrock, F., and Burrows, J. P.: Enhanced trans-Himalaya  
1121 pollution transport to the Tibetan Plateau by cut-off low systems, *Atmos. Chem. Phys.*, 17,  
1122 3083–3095, doi:10.5194/acp-17-3083-2017, 2017.

1123 Zhang, Y., Kang, S., Cong, Z., Schmale, J., Sprenger, M., Li, C., Yang, W., Gao, T., Sillanpää,  
1124 M., Li, X., Liu, Y., Chen, P., and Zhang, X.: Light-absorbing impurities enhance glacier

1125 albedo reduction in the southeastern Tibetan plateau, *J. Geophys. Res. Atmos.*, 122, 6915–  
1126 6933, doi:10.1002/2016JD026397, 2017.

1127 Zhang, Y., Kang, S., Sprenger, M., Cong, Z., Gao, T., Li, C., Tao, S., Li, X., Zhong, X., Xu,  
1128 M., Meng, W., Neupane, B., Qin, X., and Sillanpää, M.: Black carbon and mineral dust in  
1129 snow cover on the Tibetan Plateau, *The Cryosphere*, 12, 413–431, doi:10.5194/tc-12-413-  
1130 2018, 2018.

1131 Zhao, C., Chen, S., Leung, L. R., Qian, Y., Kok, J., Zaveri, R., and Huang, J.: Uncertainty in  
1132 modeling dust mass balance and radiative forcing from size parameterization, *Atmos. Chem.*  
1133 *Phys.*, 13, 10733–10753, doi:doi:10.5194/acp-13-10733-2013, 2013b.

1134 Zhao, C., Hu, Z., Qian, Y., Leung, L. R., Huang, J., Huang, M., Jin, J., Flanner, M., Zhang, R.,  
1135 Wang, H., Yan, H., Lu, Z., and Streets, D. G.: Simulating black carbon and dust and their  
1136 radiative forcing in seasonal snow: a case study over North China with field campaign  
1137 measurements, *Atmos. Chem. Phys.*, 14, 11475–11491, doi:10.5194/acp-14-11475-2014,  
1138 2014.

1139 Zhao, C., Huang, M., Fast, J. D., Berg, L. K., Qian, Y., Guenther, A., Gu, D., Shrivastava, M.,  
1140 Liu, Y., and Walters, S.: Sensitivity of biogenic volatile organic compounds to land surface  
1141 parameterizations and vegetation distributions in California, *Geosci. Model Dev*, 9, 1959–  
1142 1976, doi:10.5194/gmd-9-1959-2016, 2016.

1143 Zhao, C., Liu, X., and Leung, L. R.: Impact of the Desert dust on the summer monsoon system  
1144 over Southwestern North America, *Atmos. Chem. Phys.*, 12, 3717–3731, doi:10.5194/acp-  
1145 12-3717-2012, 2012.

1146 Zhao, C., Liu, X., Leung, L. R., and Hagos, S.: Radiative impact of mineral dust on monsoon  
1147 precipitation variability over West Africa, *Atmos. Chem. Phys.*, 11, 1879–1893,  
1148 doi:10.5194/acp-11-1879-2011, 2011.

1149 Zhao, C., Liu, X., Leung, L. R., Johnson, B., McFarlane, S. A., Gustafson, W. I., Fast, J. D.,  
1150 and Easter, R.: The spatial distribution of mineral dust and its shortwave radiative forcing  
1151 over North Africa: modeling sensitivities to dust emissions and aerosol size treatments,  
1152 *Atmos. Chem. Phys.*, 10, 8821–8838, doi:10.5194/acp-10-8821-2010, 2010.

1153 Zhao, C., Ruby Leung, L., Easter, R., Hand, J., and Avise, J.: Characterization of speciated  
1154 aerosol direct radiative forcing over California, *J. Geophys. Res. Atmos.*, 118, 2372–2388,  
1155 doi:10.1029/2012JD018364, 2013a.

1156 Zhao, P., Zhou, X., Chen, J., Liu, G., and Nan, S.: Global climate effects of summer Tibetan  
1157 Plateau, *Science Bulletin*, 64, 1–3, doi:10.1016/j.scib.2018.11.019, 2019.

1158 Zhou, X., Beljaars, A., Wang, Y., Huang, B., Lin, C., Chen, Y., and Wu, H.: Evaluation of  
1159 WRF simulations with different selections of subgrid orographic drag over the Tibetan  
1160 Plateau, *J. Geophys. Res. Atmos.*, 122, 9759–9772, doi:10.1002/2017JD027212, 2017.

1161 Zhou, X., Yang, K., and Wang, Y.: Implementation of a turbulent orographic form drag scheme  
1162 in WRF and its application to the Tibetan Plateau, *Climate dynamics*, 50, 2443–2455, doi:  
1163 10.1007/s00382-017-3677-y, 2018.

1164 Zhao, Z., Cao, J., Shen, Z., Xu, B., Zhu, C., Chen, L. W. A., Su, X., Liu, S., Han, Y., Wang,  
1165 G., and Ho, K.: Aerosol particles at a high-altitude site on the Southeast Tibetan Plateau,  
1166 China: Implications for pollution transport from South Asia, *J. Geophys. Res. Atmos.*, 118,  
1167 11,360–11,375, doi:10.1002/jgrd.50599, 2013.

1168 Zhong, S., Qian, Y., Zhao, C., Leung, R., Wang, H., Yang, B., Fan, Ji., Yan, H., Yang, X., and  
1169 Liu, D.: Urbanization-induced urban heat island and aerosol effects on climate extremes in  
1170 the Yangtze River Delta region of China, *Atmos. Chem. Phys.*, 17, 5439–5457,  
1171 doi:10.5194/acp-17-5439-2017, 2017.

1172  
1173  
1174  
1175  
1176  
1177  
1178  
1179  
1180  
1181  
1182  
1183  
1184  
1185

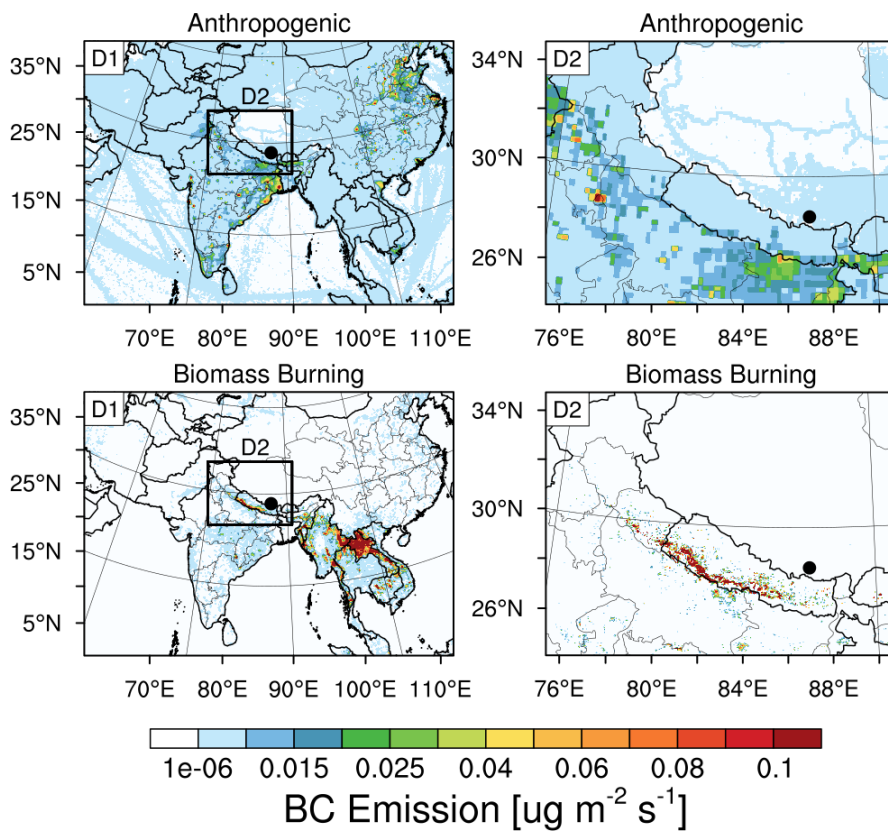
1186  
 1187  
 1188  
 1189  
 1190  
 1191  
 1192  
 1193  
 1194  
 1195

**Table 1.** Summary of model configurations.

<b>Description</b>	<b>Selection</b>	<b>References</b>
<b>Horizontal grid spacing</b>	20 km (D1), 4 km (D2)	
<b>Grid dimensions</b>	250×350, 300×400	
<b>Topography</b>	30 arcsec (USGS)	
<b>Vertical layers</b>	54 (roughly 17 layers below 2 km)	
<b>Model top pressure</b>	50 hPa	
<b>Nesting approach</b>	One-way	
<b>Aerosol scheme</b>	MOSAIC 8 bin	Zaveri et al., 2008
<b>Gas-phase chemistry</b>	CBM-Z	Zaveri and Peters, 1999
<b>Long wave Radiation</b>	RRTMG	Iacono et al., 2000; Zhao et al., 2011, 2013a
<b>Short-wave Radiation</b>	RRTMG	
<b>Cloud Microphysics</b>	Morrison 2-moment	Morrison et al., 2009
<b>Cumulus Cloud</b>	Kain-Fritsch	Kain, 2004
<b>Planetary boundary layer</b>	MYNN level 2.5	Nakanishi and Niino, 2006
<b>Land surface</b>	CLM	Oleson et al., 2010
<b>Meteorological Forcing</b>	ERA-Interim, 0.5°×0.66°, 6 hourly	

1197  
 1198  
 1199  
 1200  
 1201  
 1202  
 1203  
 1204  
 1205  
 1206  
 1207  
 1208  
 1209  
 1210  
 1211  
 1212  
 1213  
 1214  
 1215

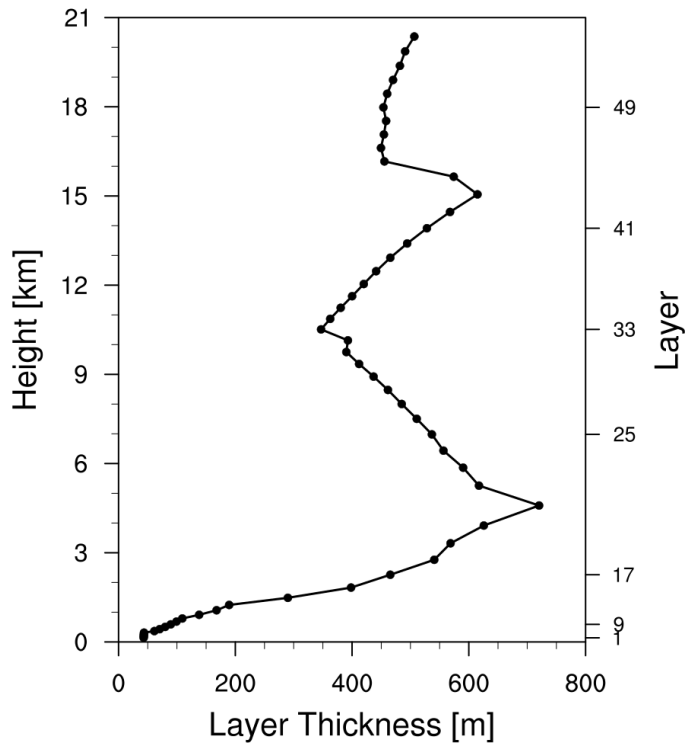
1216  
1217  
1218  
1219  
1220  
1221  
1222  
1223  
1224  
1225  
1226  
1227



1228  
1229  
1230  
1231  
1232  
1233  
1234  
1235  
1236  
1237  
1238  
1239  
1240  
1241  
1242  
1243  
1244

**Figure 1.** Anthropogenic and fire emissions over the entire simulated regions of 20-km and 4-km resolutions, the black dot represents the Qomolangma Station (QOMS, 86.95°E, 28.36°N).

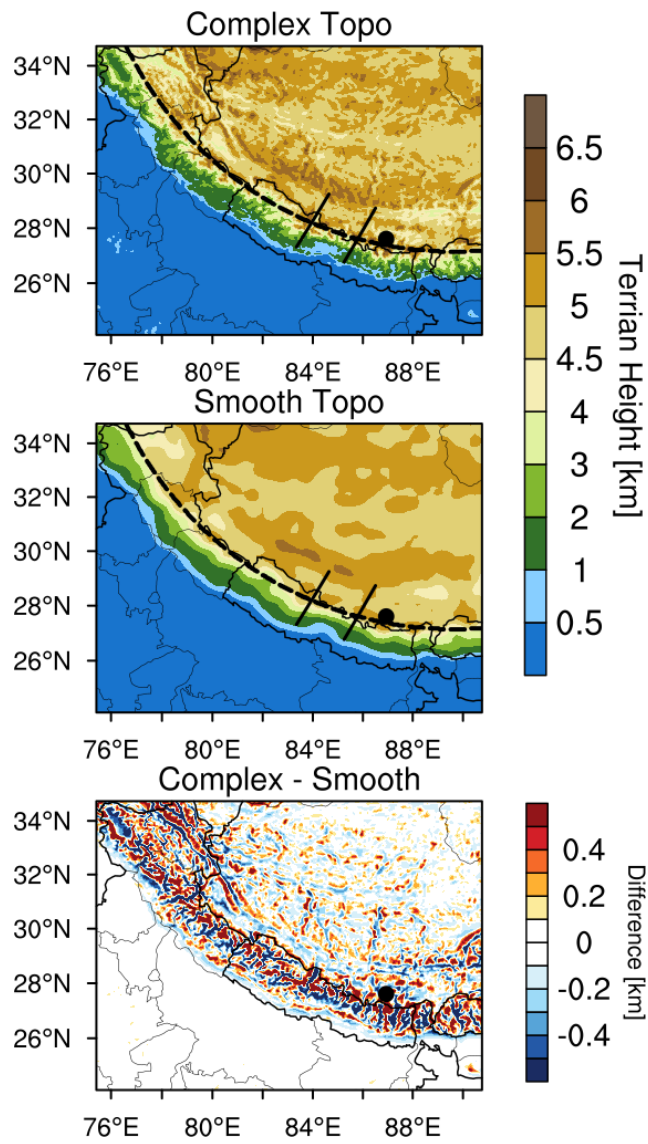
1245  
1246  
1247  
1248  
1249  
1250  
1251  
1252  
1253



1254  
1255  
1256  
1257  
1258  
1259  
1260  
1261  
1262  
1263  
1264  
1265  
1266  
1267  
1268  
1269  
1270  
1271  
1272  
1273  
1274  
1275

**Figure 2.** The thickness of each vertical layer in the simulations (54 layers in total).

1276  
1277  
1278  
1279  
1280  
1281  
1282  
1283  
1284

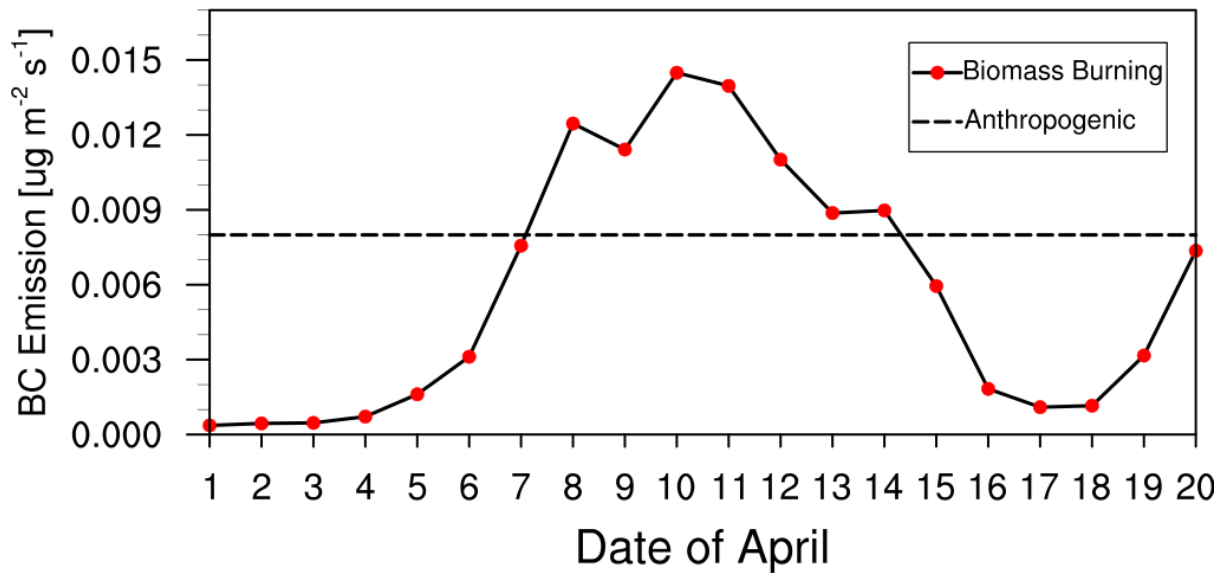


1285  
1286  
1287  
1288  
1289  
1290  
1291  
1292  
1293  
1294  
1295

**Figure 3.** Spatial distributions of terrain height from the dataset at 4-km resolution (Complex Topo) and bilinearly interpolated from the 20-km resolution dataset (Smooth Topo). The one dash line and two solid lines represent the cross sections for analysis in the following.



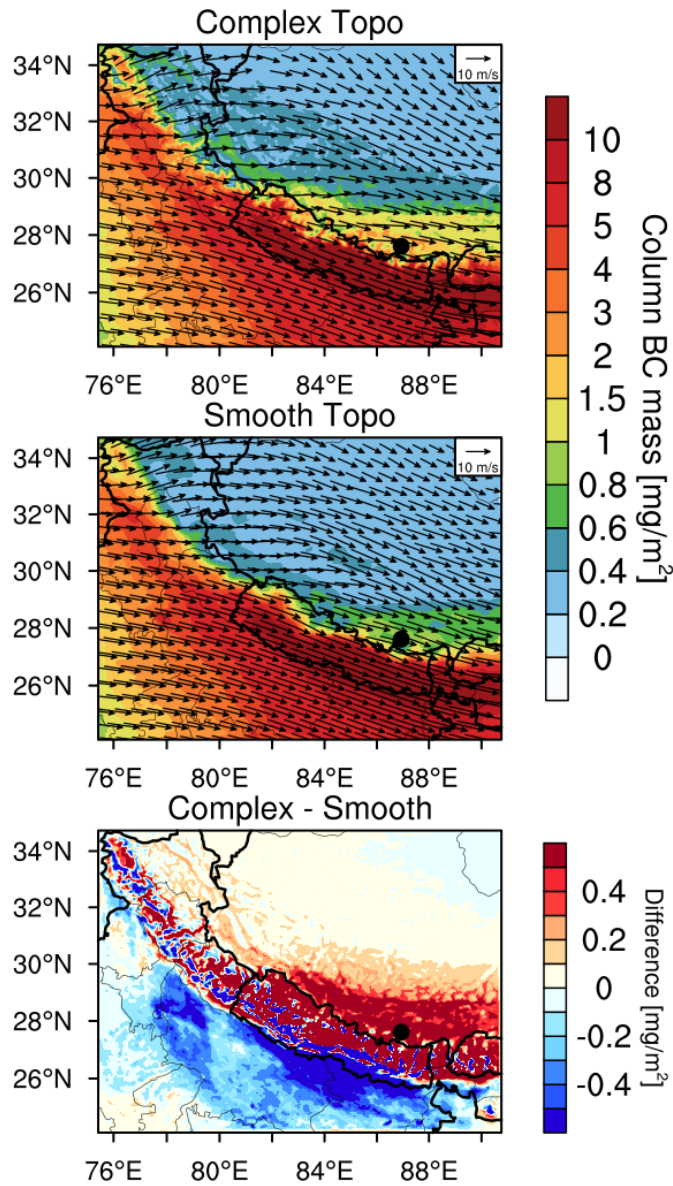
1296  
1297  
1298  
1299  
1300  
1301  
1302  
1303  
1304



1305  
1306  
1307  
1308  
1309  
1310  
1311  
1312  
1313  
1314  
1315  
1316  
1317  
1318  
1319  
1320  
1321  
1322  
1323  
1324  
1325  
1326  
1327  
1328  
1329  
1330  
1331

**Figure 4.** Time series of area-averaged daily fire emissions between 26°N and 29°N over the simulation domain at 4-km resolution (The dash line in the figure represents the anthropogenic emissions).

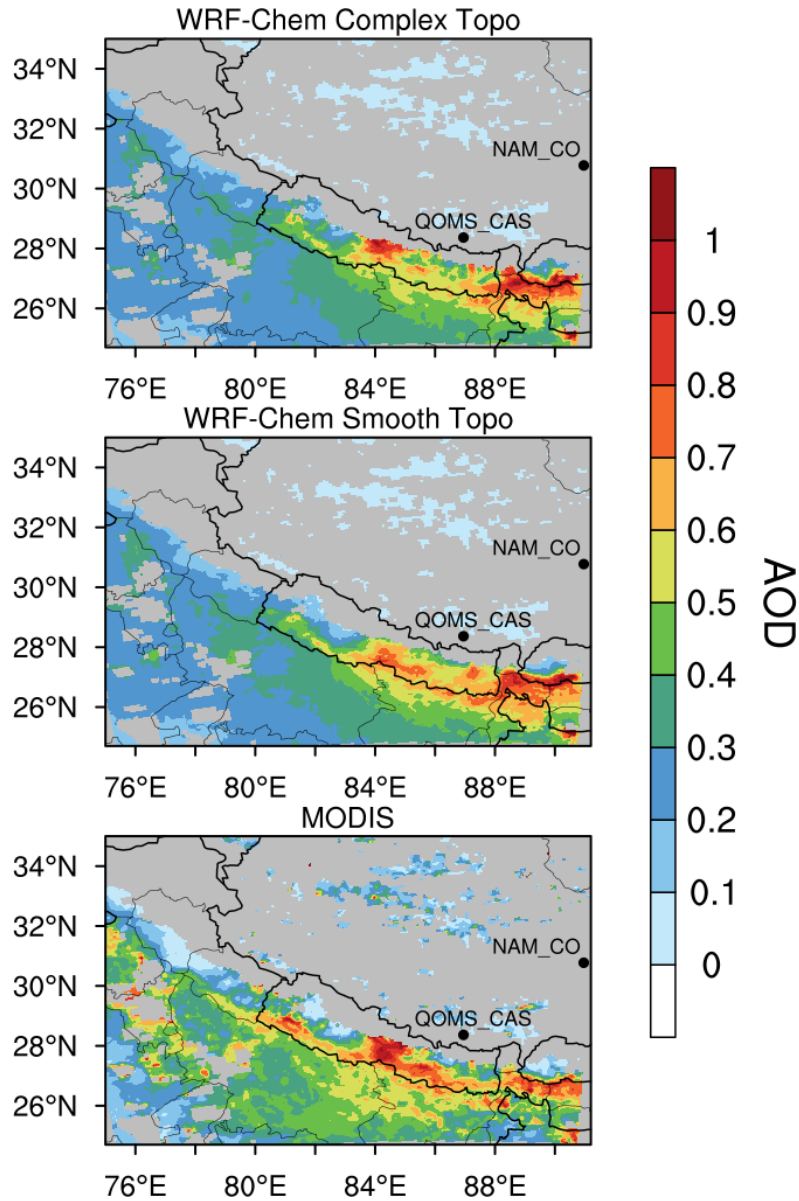
1332  
1333  
1334  
1335  
1336



1337  
1338  
1339  
1340  
1341  
1342  
1343  
1344  
1345  
1346  
1347  
1348  
1349  
1350

**Figure 5.** Spatial distributions of column integrated BC mass and the horizontal wind field at 500 hPa from the simulations with complex and smooth topography (Complex Topo and Smooth Topo) averaged for April 1-20, 2016. The difference between the two is also shown.

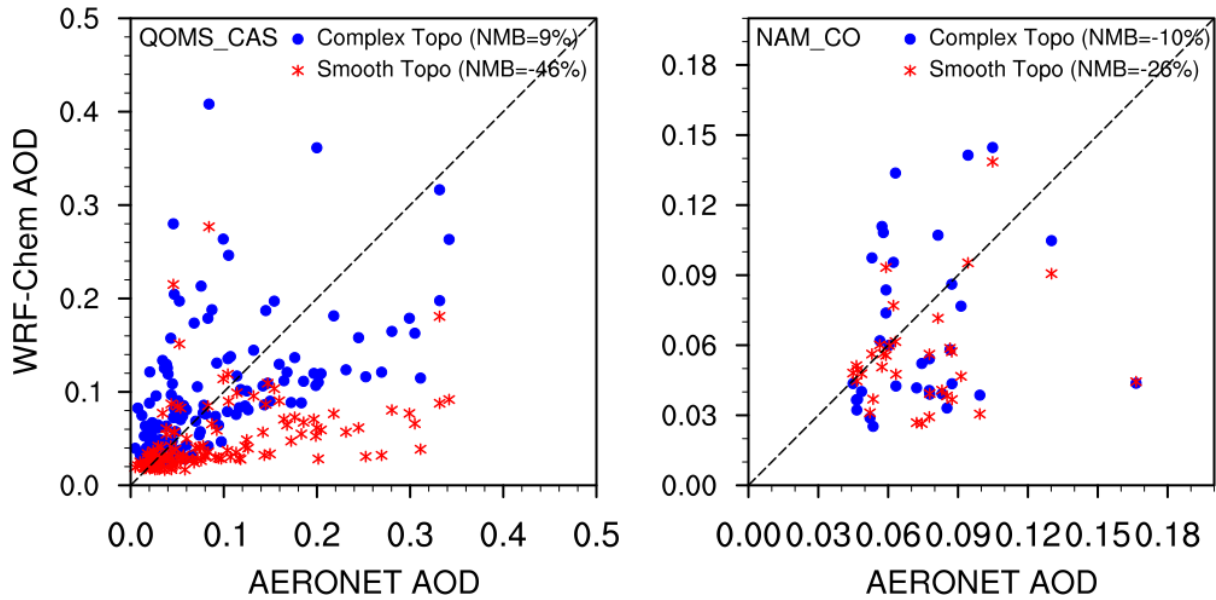
1351  
1352  
1353  
1354  
1355  
1356  
1357



1358  
1359  
1360  
1361  
1362  
1363  
1364  
1365  
1366  
1367  
1368  
1369

**Figure 6.** Spatial distributions of AOD from the MODIS retrievals and the simulations with complex and smooth topography averaged for April 1-20, 2016. The two black dots represent the two AERONET sites over the TP (QOMS\_CAS, 86.95°E, 28.36°N; NAM\_CO, 90.96°E, 30.77°N).

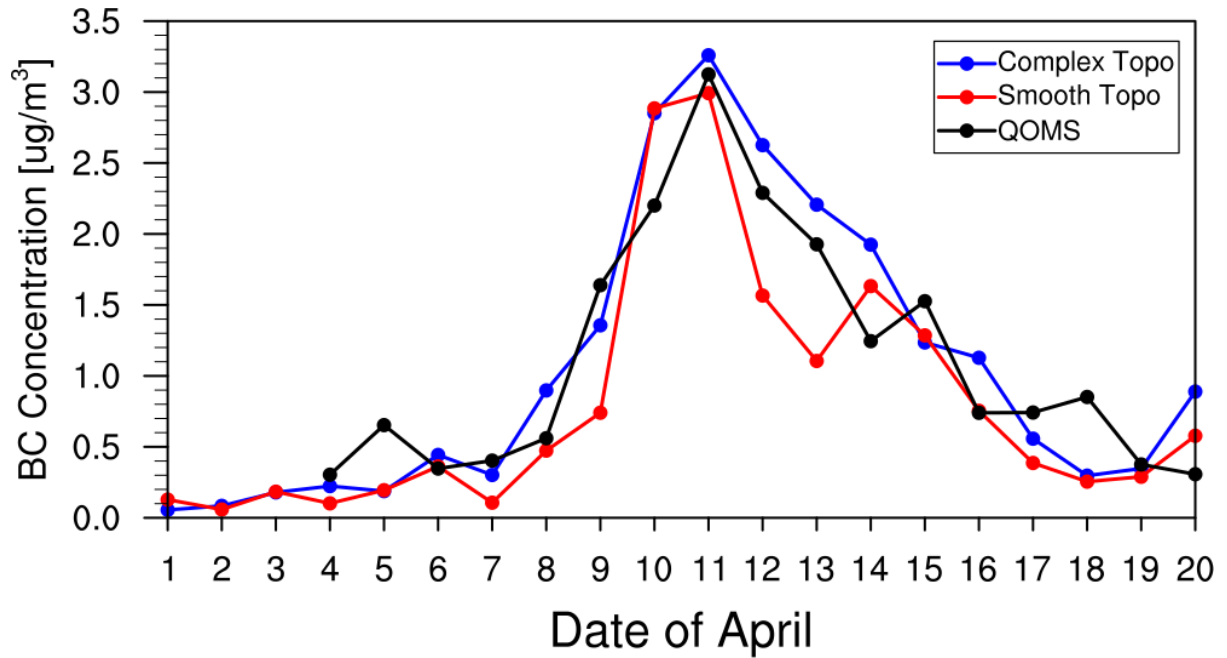
1370  
1371  
1372  
1373  
1374  
1375  
1376  
1377



1378  
1379  
1380  
1381  
1382  
1383  
1384  
1385  
1386  
1387  
1388  
1389  
1390  
1391  
1392  
1393  
1394  
1395  
1396  
1397  
1398  
1399  
1400  
1401  
1402  
1403

**Figure 7.** Hourly AOD from the measurements of AERONET and simulations by WRF-Chem at the two sites over the TP (QOMS\_CAS, 86.95°E, 28.36°N; NAM\_CO, 90.96°E, 30.77°N) for April 1-20, 2016.

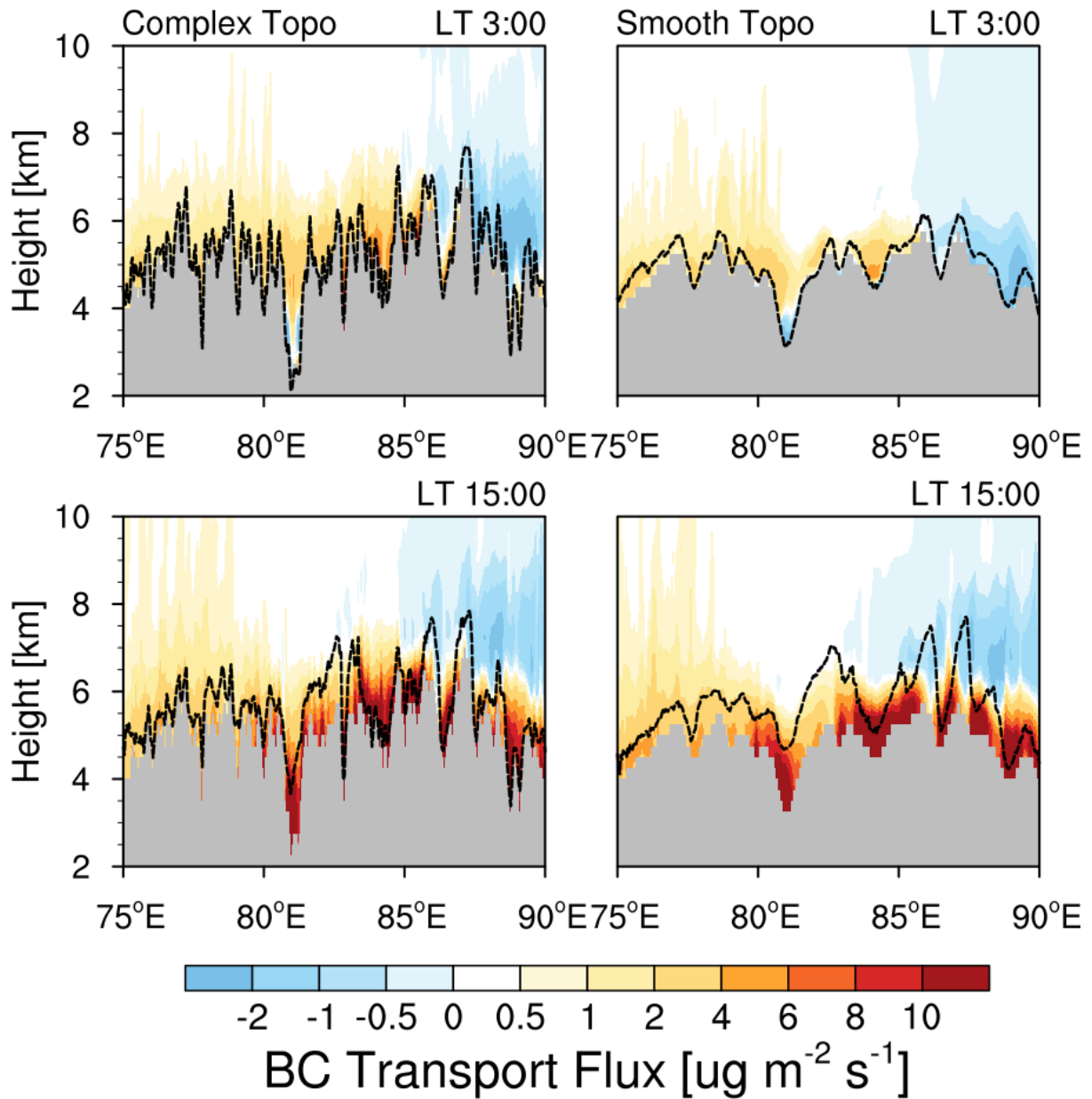
1404  
1405  
1406  
1407  
1408  
1409  
1410



1411  
1412  
1413  
1414  
1415  
1416  
1417  
1418  
1419  
1420  
1421  
1422  
1423  
1424  
1425  
1426  
1427  
1428  
1429  
1430  
1431  
1432  
1433  
1434  
1435  
1436

**Figure 8.** The simulated (colored) and observed (black) temporal variability of surface BC mass concentration at the measurement station during April 1-20 in 2016.

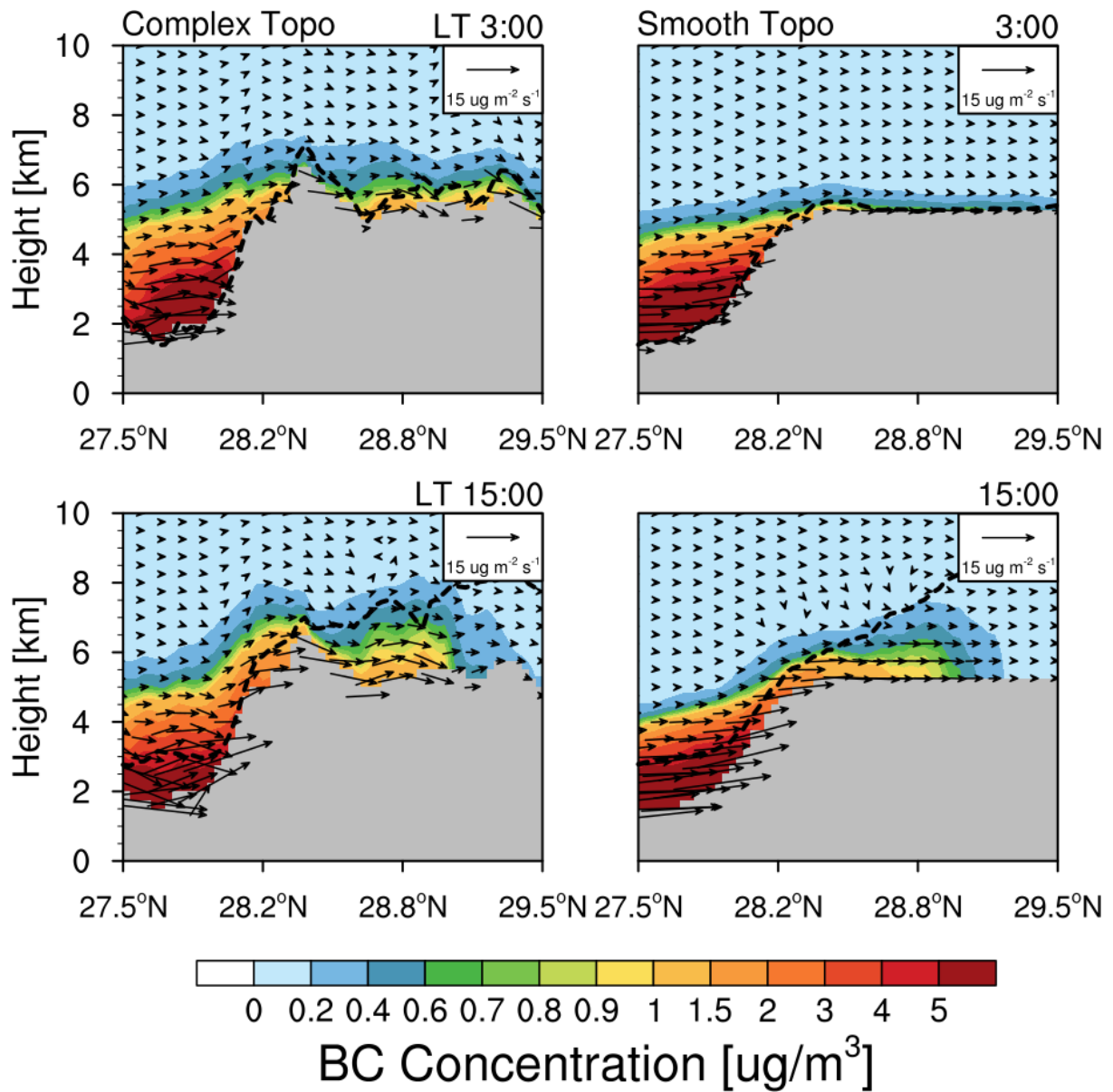
1437  
1438  
1439  
1440  
1441  
1442  
1443



1444  
1445  
1446  
1447  
1448  
1449  
1450  
1451  
1452  
1453  
1454

**Figure 9.** Longitude-height cross section of BC transport flux along the cross line (shown as the black dash line in Fig. 3) from the simulations with complex and smooth topography at local time (LT) 03:00 and 15:00 averaged for April 1-20. The PBL height along the cross section is shown here as the black dash line.

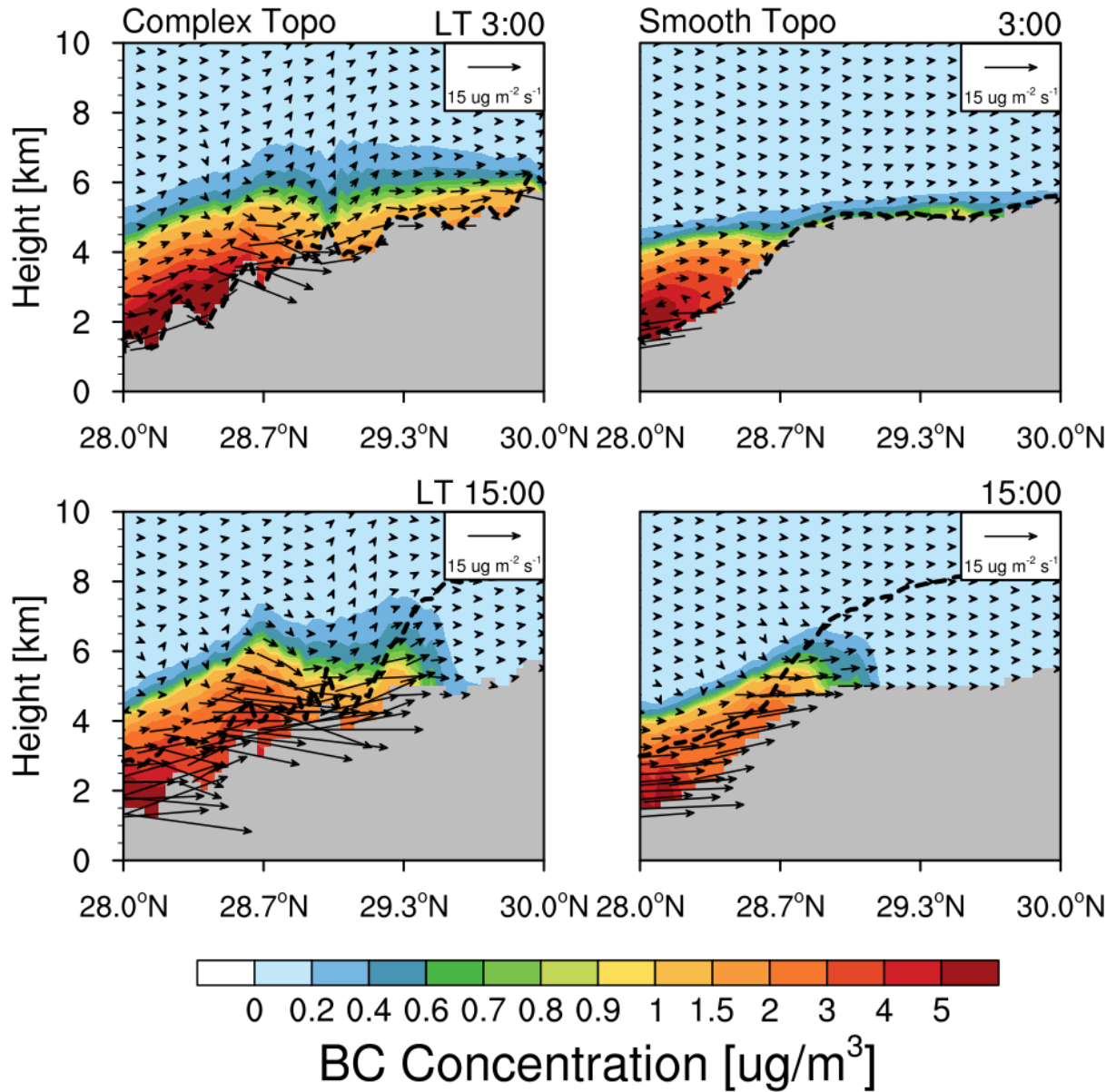
1455  
1456  
1457  
1458  
1459  
1460  
1461  
1462  
1463



1464  
1465  
1466  
1467  
1468  
1469  
1470  
1471  
1472  
1473

**Figure 10.** Latitude-height cross section of BC flux (vector) across the mountain (shown as the East black solid line in Fig.3) from the simulations with complex and smooth topography at local time (LT) 03:00 and 15:00 averaged for April 1-20, 2016. Contour represents the BC concentration.

1474  
1475  
1476  
1477  
1478  
1479  
1480

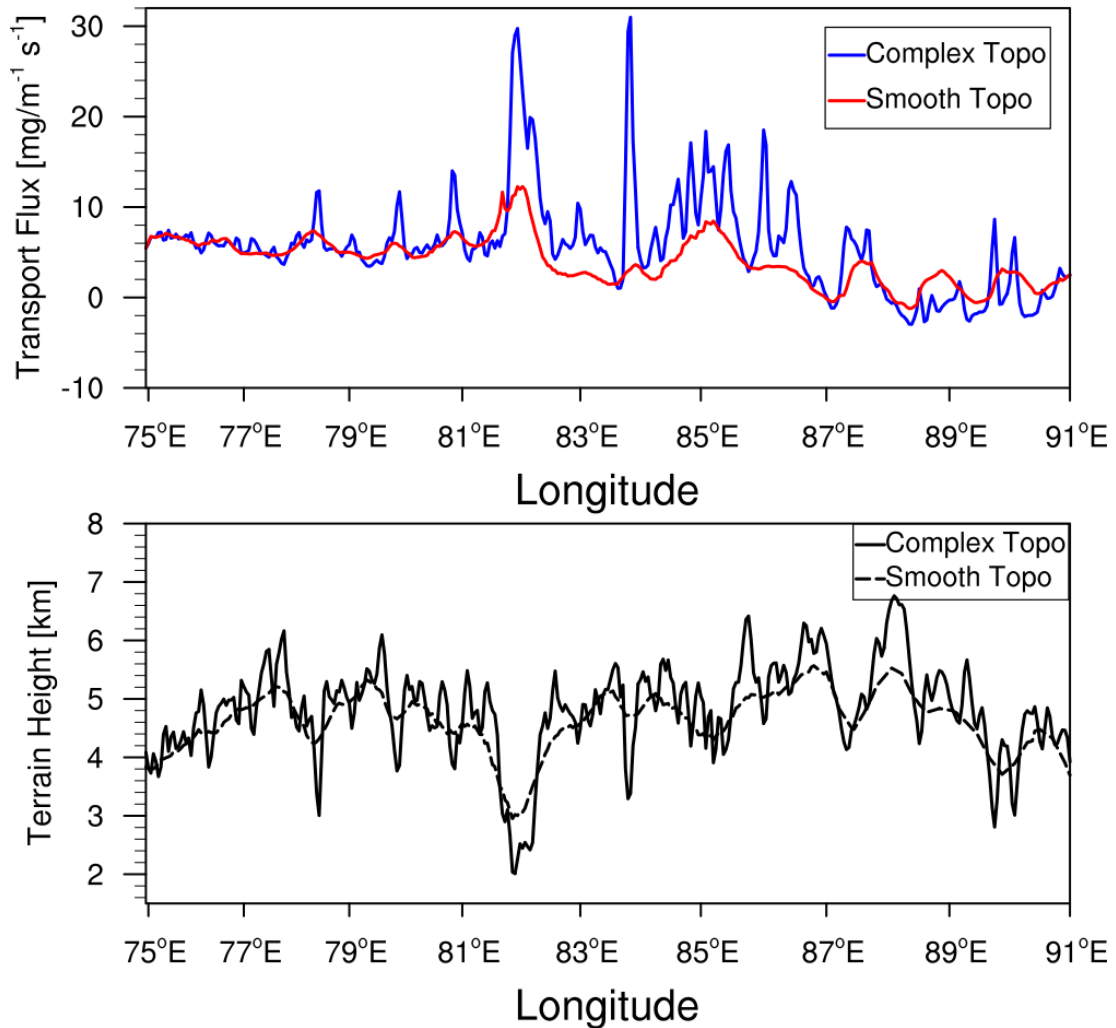


1481  
1482  
1483  
1484  
1485  
1486  
1487  
1488  
1489  
1490  
1491  
1492

**Figure 11.** Latitude-height cross section of BC flux (vector) along the valley (shown as the West black solid line in Fig. 3) from the simulations with complex and smooth topography at local time (LT) 03:00 and 15:00 averaged for April 1-20, 2016. Contour represents the BC concentration.



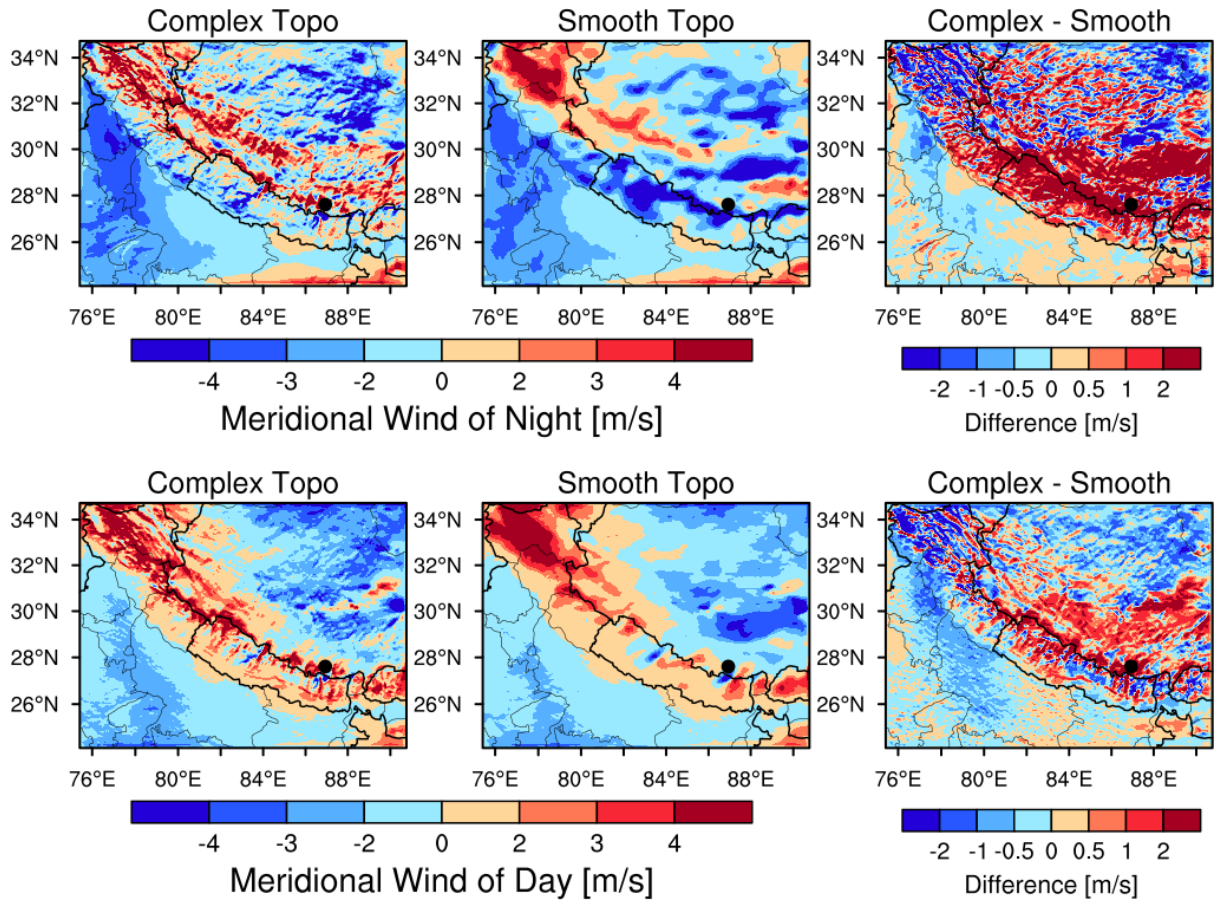
1493  
1494  
1495  
1496



1497  
1498  
1499  
1500  
1501  
1502  
1503  
1504  
1505  
1506  
1507  
1508  
1509  
1510  
1511  
1512  
1513  
1514  
1515

**Figure 12.** Longitudinal distribution of integrated BC mass flux along the cross section in Fig. 3 from the simulations with complex and smooth topography. The black lines represent the terrain heights with different topography.

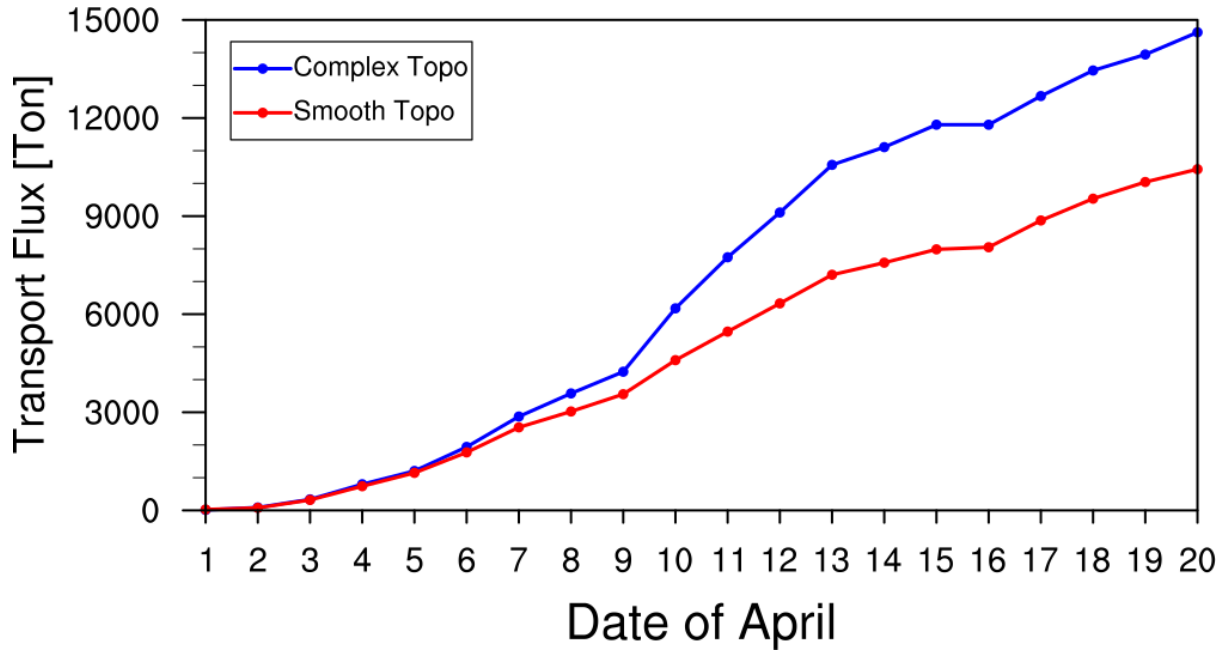
1516  
1517  
1518  
1519  
1520  
1521  
1522



1523  
1524  
1525  
1526  
1527  
1528  
1529  
1530  
1531  
1532  
1533  
1534  
1535  
1536  
1537  
1538  
1539  
1540  
1541  
1542

**Figure 13.** Spatial distributions of meridional wind speed averaged within 500 m above the ground for day and night during April 1-20, 2016 from the simulations with complex and smooth topography. The difference between the two is also shown. Nighttime is defined as local time 21:00-6:00, and daytime is defined as 9:00-18:00. Positive value denotes southerly, and negative value denotes northerly.

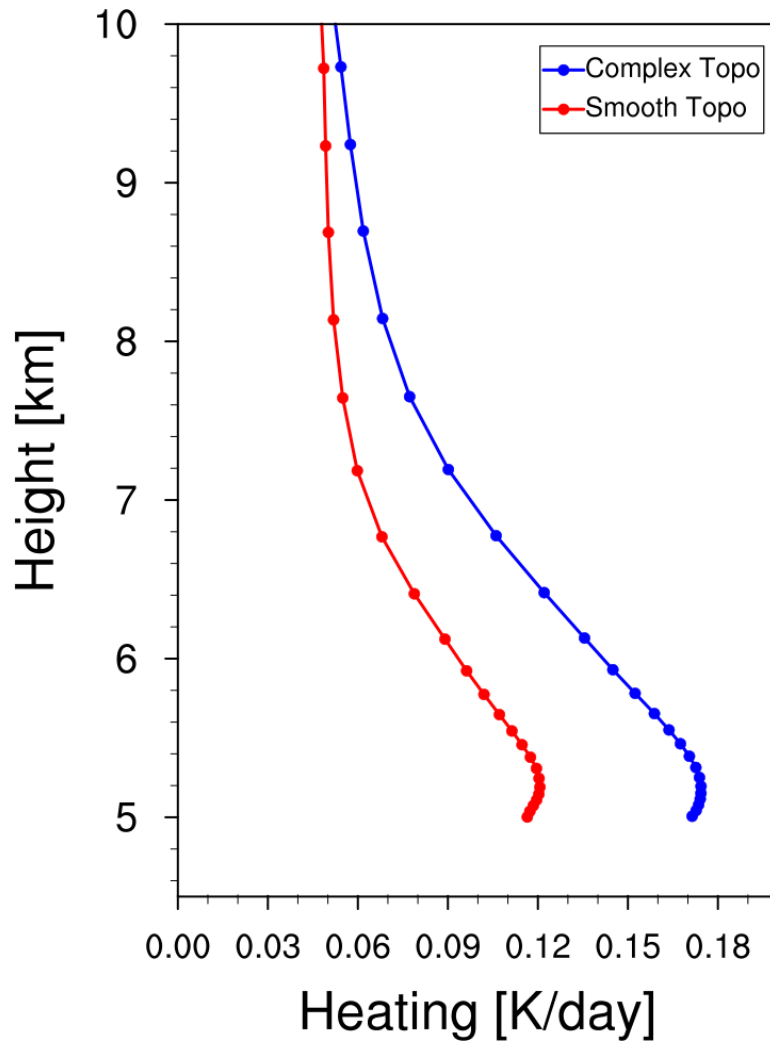
1543  
1544  
1545  
1546  
1547



1548  
1549  
1550  
1551  
1552  
1553  
1554  
1555  
1556  
1557  
1558  
1559  
1560  
1561  
1562  
1563  
1564  
1565  
1566  
1567  
1568  
1569  
1570  
1571  
1572  
1573  
1574  
1575  
1576

**Figure 14.** Accumulated integrated total transport flux of BC across the Himalayas estimated from the simulations with complex and smooth topography during April 1-20, 2016.

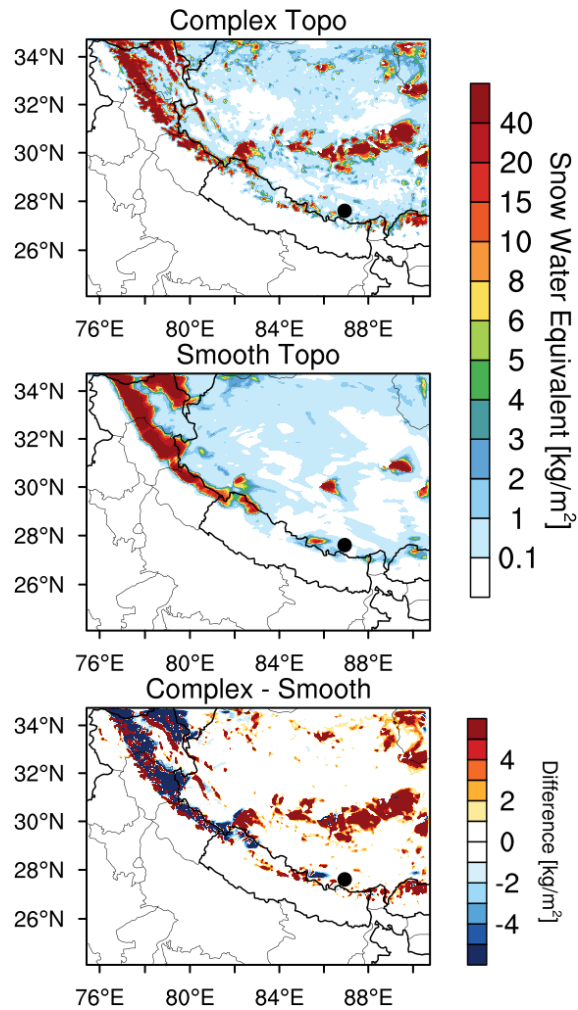
1577  
1578  
1579  
1580  
1581



1582  
1583  
1584  
1585  
1586  
1587  
1588  
1589  
1590  
1591  
1592  
1593  
1594  
1595  
1596  
1597  
1598  
1599

**Figure 15.** Vertical profiles of BC induced radiative heating rate in the atmosphere averaged over the TP (with elevation > 4 km) from the simulations with complex and smooth topography during April 1-20, 2016.

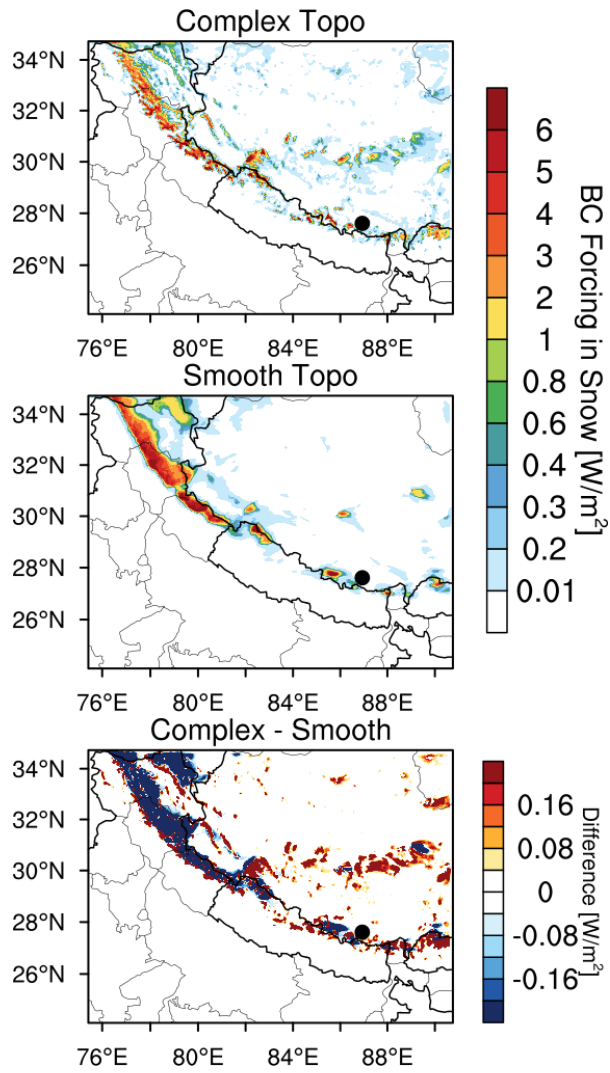
1600  
1601  
1602  
1603  
1604



1605  
1606 **Figure 16.** Spatial distributions of snow water equivalent averaged for April 1-20, 2016 from  
1607 the simulations with complex and smooth topography. The difference between the two is also  
1608 shown.

1609  
1610  
1611  
1612  
1613  
1614  
1615  
1616  
1617  
1618  
1619  
1620  
1621  
1622  
1623

1624  
1625  
1626  
1627  
1628



1629  
1630  
1631  
1632  
1633  
1634  
1635  
1636  
1637  
1638  
1639  
1640

**Figure 17.** Spatial distributions of BC radiative forcing in the surface snow averaged for April 1-20, 2016 from the simulations with complex and smooth topography. The difference between the two is also shown.